Kepler-20: A Sun-like Star with Three Sub-Neptune Exoplanets and Two Earth-size Candidates

The Astrophysical Journal, 749:15 (19pp), 2012 April 10 doi:10.1088/0004-637X/749/1/15

KEPLER-20: A SUN-LIKE STAR WITH THREE SUB-NEPTUNE EXOPLANETS AND TWO EARTH-SIZE CANDIDATES

Thomas N. Gautier III[1], David Charbonneau[2], Jason F. Rowe[3], Geoffrey W. Marcy[4], Howard Isaacson[4], Guillermo Torres[2], Francois Fressin[2], Leslie A. Rogers[5], Jean-Michel Désert[2], Lars A. Buchhave[6,7], David W. Latham[2], Samuel N. Quinn[2], David R. Ciardi[8], Daniel C. Fabrycky[9], Eric B. Ford[10], Ronald L. Gilliland[11], Lucianne M. Walkowicz[12], Stephen T. Bryson[3], William D. Cochran[13], Michael Endl[13], Debra A. Fischer[14], Steve B. Howell[3], Elliott P. Horch[15], Thomas Barclay[16], Natalie Batalha[17], William J. Borucki[3], Jessie L. Christiansen[3], John C. Geary[2], Christopher E. Henze[3], Matthew J. Holman[2], Khadeejah Ibrahim[3], Jon M. Jenkins[18], Karen Kinemuchi[16], David G. Koch[3], Jack J. Lissauer[3], Dwight T. Sanderfer[3], Dimitar D. Sasselov[2], Sara Seager[5], Kathryn Silverio[4], Jeffrey C. Smith[18], Martin Still[16], Martin C. Stumpe[18], Peter Tenenbaum[18], and Jeffrey Van Cleve[18]

[1] Jet Propulsion Laboratory/California Institute of Technology, Pasadena, CA 91109, USA; thomas.n.gautier@jpl.nasa.gov
[2] Harvard-Smithsonian Center for Astrophysics, Cambridge, MA 02138, USA
[3] NASA Ames Research Center, Moffett Field, CA 94035, USA
[4] Department of Astronomy, University of California, Berkeley, CA 94720, USA
[5] Department of Physics, Massachusetts Institute of Technology, Cambridge, MA 02139, USA
[6] Niels Bohr Institute, University of Copenhagen, DK-2100, Copenhagen, Denmark
[7] Centre for Star and Planet Formation, Natural History Museum of Denmark, University of Copenhagen, DK-1350, Copenhagen, Denmark
[8] NASA Exoplanet Science Institute/California Institute of Technology, Pasadena, CA 91125, USA
[9] Department of Astronomy and Astrophysics, University of California, Santa Cruz, CA 95064, USA
[10] Astronomy Department, University of Florida, Gainesville, FL 32111, USA
[11] Department of Astronomy, 525 Davey Lab, The Pennsylvania State University, University Park, PA 16802, USA
[12] Department of Astrophysical Sciences, Princeton University, Princeton, NJ 08544, USA
[13] McDonald Observatory, The University of Texas at Austin, Austin, TX 78712, USA
[14] Department of Astronomy, Yale University, New Haven, CT 06511, USA
[15] Department of Physics, Southern Connecticut State University, New Haven, CT 06515, USA
[16] Bay Area Environmental Research Institute/NASA Ames Research Center, Moffett Field, CA 94035, USA
[17] Department of Physics and Astronomy, San Jose State University, San Jose, CA 95192, USA
[18] SETI Institute/NASA Ames Research Center, Moffett Field, CA 94035, USA
Received 2011 November 28; accepted 2011 December 19; published 2012 March 16

ABSTRACT

We present the discovery of the Kepler-20 planetary system, which we initially identified through the detection of five distinct periodic transit signals in the *Kepler* light curve of the host star 2MASS J19104752+4220194. From high-resolution spectroscopy of the star, we find a stellar effective temperature $T_{\rm eff} = 5455 \pm 100$ K, a metallicity of [Fe/H] $= 0.01 \pm 0.04$, and a surface gravity of $\log g = 4.4 \pm 0.1$. We combine these estimates with an estimate of the stellar density derived from the transit light curves to deduce a stellar mass of $M_\star = 0.912 \pm 0.034\ M_\odot$ and a stellar radius of $R_\star = 0.944^{+0.060}_{-0.095}\ R_\odot$. For three of the transit signals, we demonstrate that our results strongly disfavor the possibility that these result from astrophysical false positives. We accomplish this by first identifying the subset of stellar blends that reproduce the precise shape of the light curve and then using the constraints on the presence of additional stars from high angular resolution imaging, photometric colors, and the absence of a secondary component in our spectroscopic observations. We conclude that the planetary scenario is more likely than that of an astrophysical false positive by a factor of 2×10^5 (Kepler-20b), 1×10^5 (Kepler-20c), and 1.1×10^3 (Kepler-20d), sufficient to validate these objects as planetary companions. For Kepler-20c and Kepler-20d, the blend scenario is independently disfavored by the achromaticity of the transit: from *Spitzer* data gathered at 4.5 μm, we infer a ratio of the planetary to stellar radii of 0.075 ± 0.015 (Kepler-20c) and 0.065 ± 0.011 (Kepler-20d), consistent with each of the depths measured in the *Kepler* optical bandpass. We determine the orbital periods and physical radii of the three confirmed planets to be 3.70 days and $1.91^{+0.12}_{-0.21}\ R_\oplus$ for Kepler-20b, 10.85 days and $3.07^{+0.20}_{-0.31}\ R_\oplus$ for Kepler-20c, and 77.61 days and $2.75^{+0.17}_{-0.30}\ R_\oplus$ for Kepler-20d. From multi-epoch radial velocities, we determine the masses of Kepler-20b and Kepler-20c to be $8.7 \pm 2.2\ M_\oplus$ and $16.1 \pm 3.5\ M_\oplus$, respectively, and we place an upper limit on the mass of Kepler-20d of $20.1\ M_\oplus$ (2σ).

Key words: eclipses – planetary systems – stars: individual (Kepler-20, KIC 6850504, 2MASS J19104752+4220194)

Online-only material: color figures, machine-readable table

1. INTRODUCTION

Systems with multiple exoplanets, and transiting exoplanets, each bolster confidence in the reality of the planetary interpretation of the signals and offer distinct constraints on models of planet formation.

The first extrasolar planets were found around a pulsar (Wolszczan & Frail 1992), and it was the multi-planetary nature—in particular the gravitational perturbations between the planets (Rasio et al. 1992; Wolszczan 1994)—that solidified this outlandish claim. Around Sun-like stars as well, the origin of radial velocity (RV) signals continued to be questioned by some;

at the time multiple planets were found around υ Andromeda (Butler et al. 1999). The orbital configuration of planets relative to each other has shed light on a host of physical processes, from smooth radial migration into resonant orbits (Lee & Peale 2002) to chaotic scattering into secular eccentricity cycles (Malhotra 2008; Ford et al. 2005). Now with ever-growing statistics of ever-smaller Doppler-detected planets in multiple systems (Mayor et al. 2011), the formation and early history of planetary systems continue to come into sharper focus.

Concurrently, transiting exoplanets have paid burgeoning dividends, starting with the definitive proof that Doppler signals were truly due to gas-giant planets orbiting in close-in orbits (Charbonneau et al. 2000; Henry et al. 2000). Transit light curves offer precise geometrical constraints on the orbit of the planet (Winn 2010), such that RV and photometric measurements yield the density of the planet and hence point to its composition (Adams et al. 2008; Miller & Fortney 2011). Transiting configurations also enable follow-up measurements (Charbonneau et al. 2002; Knutson et al. 2007; Triaud et al. 2010) that inform on the mechanisms of planetary formation, evolution, and even weather.

These two research streams, multi-planets and transiting planets, came together for the first time with the discovery of Kepler-9 (Holman et al. 2010; Torres et al. 2011). This discovery was enabled by data from the *Kepler Mission* (Borucki et al. 2010; Koch et al. 2010), which is uniquely suited for such detections as it offers near-continuous high-precision photometric monitoring of target stars. Based on the first 4 months of *Kepler* data, Borucki et al. (2011) announced the detection of 170 stars each with two or more candidate transiting planets; Steffen et al. (2010) discussed in detail five systems each possessing multiple candidate transiting planets. A comparative analysis of the population of candidates with multiple planets and single planets was published by Latham et al. (2011), and Lissauer et al. (2011b) discussed the architecture and dynamics of the ensemble of candidate multi-planet systems.

The path to confirming the planetary nature of such *Kepler* candidates is arduous. At present, three stars (in addition to Kepler-9) hosting multiple transiting candidates have been presented in detail, and the planetary nature of each of the candidates has been established: these systems are Kepler-10 (Batalha et al. 2011; Fressin et al. 2011), Kepler-11 (Lissauer et al. 2011a), and Kepler-18 (Cochran et al. 2011). Transiting planets are most profitable when their masses can be determined directly from observation, either through RV monitoring of the host star or by transit timing variations (TTVs), as was done for Kepler-9bc, Kepler-10b, Kepler-11bcdef, and Kepler-18bcd. When neither the RV nor TTV signals are detected, statistical arguments can be employed to show that the planetary hypothesis is far more likely than alternate scenarios (namely, blends of several stars containing an eclipsing component), and this was the means by which Kepler-9d, Kepler-10c, and Kepler-11g were all validated. While such work proves the existence of a planet and determines its radius, the mass and hence composition remain unknown save for speculation from theoretical considerations.

This paper presents the discovery of a new system, Kepler-20, with five candidate transiting planets. We validate three of these by statistical argument; we then proceed to use RV measurements to determine the masses of two of these, and we place an upper limit on the mass of the third. We do not validate in this paper the remaining two signals (and hence they remain only candidates, albeit very interesting ones, owing to their diminutive sizes); rather, the validation of these two remaining signals is addressed in a separate effort (Fressin et al. 2012b). The paper is structured as follows: In Section 2, we present our extraction of the *Kepler* light curve (Section 2.1), our modeling of these data (and RVs) to estimate the orbital and physical parameters of the planets and star (Section 2.2), limits on the motion of the photocentroid during transit (Section 2.3), and a study of the long-term astrophysical variability of the star from the *Kepler* light curve (Section 2.4). In Section 3, we present follow-up observations that we use to argue for the planetary interpretation, including high-resolution imaging (Section 3.1) and *Spitzer* photometry (Section 3.2), and the spectroscopy we use to characterize the star and determine the RV signal (Section 3.3). In Section 4, we present our statistical analysis that validates the planetary nature of the three largest candidate planets in the system. In Section 5, we consider the dynamics of the system, and in Section 6 we discuss the constraints on the composition and formation history of the three planets.

1.1. Nomenclature

Throughout the course of the *Kepler Mission*, a given star is known by many different names (see Borucki et al. 2011 for an explanation of *Kepler* naming conventions), and we pause here to explain the relationship of these names in the current context. The star that is the subject of this paper is located at $\alpha = 19^{\rm h}10^{\rm m}47\overset{\rm s}{.}52$, $\delta = +42^\circ 20' 19\overset{''}{.}4$ (J2000). It was already known as 2MASS J19104752+4220194, and in the *Kepler* Input Catalog (KIC) it was designated as KIC 6850504. After the identification of candidate transiting planets it became a *Kepler* Object of Interest (KOI) and was further dubbed K00070, and it appeared as such in the list of candidates published by Borucki et al. (2011). Some authors have elected to denote KOIs using a different nomenclature, in which case K00070 would be identified as KOI-70. After the confirmation of the planetary nature of three of these candidates, it was given its final moniker, Kepler-20. This paper describes that process of confirmation, but for simplicity we refer to the star as Kepler-20 throughout. The three confirmed exoplanets were initially assigned KOI designations representing the chronological order in which the transiting signals were identified, but to avoid confusion we will refer to them henceforth by their Kepler-20 designations in which they are ordered by increasing orbital period P: Kepler-20b (K00070.02, $P = 3.70$ days), Kepler-20c (K00070.01, $P = 10.85$ days), and Kepler-20d (K00070.03, $P = 77.61$ days). We will refer to the two remaining candidates as K00070.04 and K00070.05, but note (as described below) that the period of K00070.04 ($P = 6.10$ days) is intermediate between those of Kepler-20b and Kepler-20c, and the period of K00070.05 ($P = 19.58$ days) is intermediate between those of Kepler-20c and Kepler-20d.

2. *KEPLER* PHOTOMETRY AND ANALYSIS

2.1. Light-curve Extraction

Kepler observations of Kepler-20 commenced UT 2009 May 13 with Quarter 1 (Q1), and the *Kepler* data that we describe here extend through UT 2011 March 14, corresponding to the end of Quarter 8 (Q8), resulting in near-continuous monitoring over a span of 22.4 months. The *Kepler* bandpass spans 423–897 nm, for which the response is greater than 5% (Van Cleve & Caldwell 2009). This wavelength domain is roughly equivalent to the

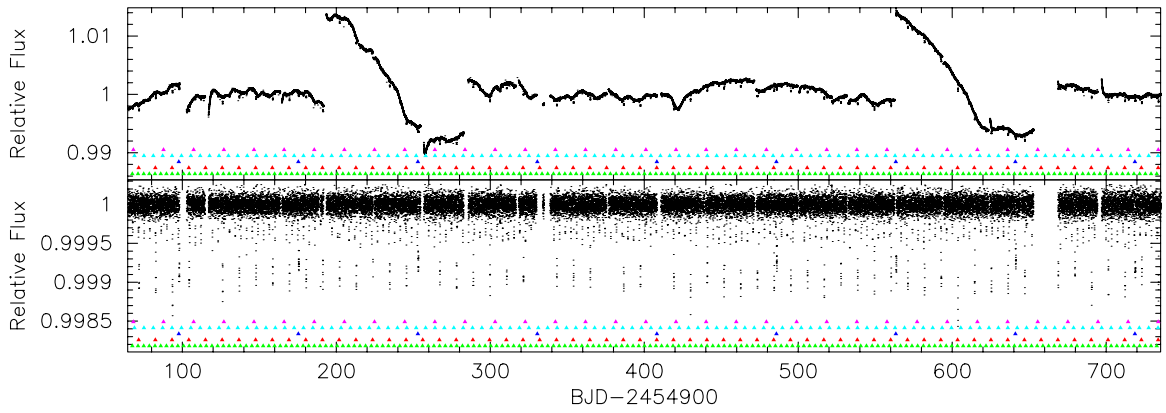

Figure 1. *Kepler* light curve of Kepler-20 at a cadence of 30 minutes. Upper panel: the normalized raw SAP light curves for Q1−Q8. The star is positioned on one of four different detectors, depending on the particular quarter, which results in the most obvious offsets that occur roughly four times per year. The other discontinuities are due to effects such as spacecraft safe-mode events and loss of fine pointing. Lower panel: the SAP light curve after removing instrumental and long-term astrophysical variability via polynomial fitting (see Section 2.2). In both panels transits of Kepler-20b are marked in green, 20c in red, 20d in blue, K00070.04 in cyan, and K00070.05 in magenta.

(A color version of this figure is available in the online journal.)

$V+R$ band (Koch et al. 2010). These observations have been reduced and calibrated by the *Kepler* pipeline (Jenkins et al. 2010b). The *Kepler* pipeline produces calibrated light curves referred to as Simple Aperture Photometry (SAP) data in the *Kepler* archive, and this is the data product we used as the initial input for our analysis to determine the system parameters (see below). The pipeline provides time series with times in Barycentric Julian days (BJD) and flux in photoelectrons per observation. The data were initially gathered at long cadence (Caldwell et al. 2010; Jenkins et al. 2010c), consisting of an integration time per data point of 29.426 minutes. After the identification of candidate transiting planets in the data from Q1, the target was also observed at short cadence (Gilliland et al. 2010), corresponding to an integration time of 1 minute for Q2−Q6. We elected to use the long-cadence version of the entire Q1−Q8 time series for computational efficiency. There are 29,595 measurements in the Q1−Q8 time series. The upper panel of Figure 1 shows the raw *Kepler* Q1−Q8 light curve of Kepler-20. The data are available electronically from the Multi Mission Archive at the Space Telescope Science Institute Web site.[19]

2.2. Derivation of System Parameters

The five candidate transiting planets that are the subject of the paper were identified by the procedure described in Borucki et al. (2011). Four of them (Kepler-20b, Kepler-20c, Kepler-20d, K00070.04) are listed in that paper, and K00070.05 was detected subsequently.

We first cleaned the Q1−Q8 long-cadence *Kepler* SAP photometry of Kepler-20 of instrumental and long-term astrophysical variability not related to the planetary transits by fitting and removing a second-order polynomial to each contiguous photometric segment. We defined a segment to be a series of long-cadence observations that does not have a gap larger than five measurements (spanning at least 2.5 hr). In this process, we gave no statistical weight to observations that fell within a transit. We then normalized the corrected light curve by its median, and this cleaned light curve is displayed in the lower panel of Figure 1.

We then modeled simultaneously both this cleaned photometric time series and the RV measurements (described below in Section 3.3 and listed in Table 5) to estimate the orbital and physical parameters of the star and its candidate planets. The free parameters in the fit were the mean stellar density $\rho_\star$ and the RV instrumental zero point γ, and seven parameters for each of the five planet candidates $i = \{$Kepler-20b, Kepler-20c, Kepler-20d, K00070.04, K00070.05$\}$, namely, the epoch of center of transit $T_{0,i}$, the orbital period P_i, the impact parameter b_i, the ratio of the planetary and stellar radii $(R_p/R_\star)_i$, the RV semi-amplitude K_i, and the two quantities $(e\ \cos\omega)_i$ and $(e\ \sin\omega)_i$ relating the eccentricity e_i and the argument of pericenter ω_i. The ratios of the semimajor axes to the stellar radius, $(a/R_\star)_i$, were calculated from $\rho_\star$ and the orbital periods P_i assuming $e = 0$ and that $M_\star \gg$ sum of the planet masses. (We note that our observations do not constrain the eccentricity, but we include it so that our error estimates of the other parameters are inflated to account for this possibility. Similarly, we are not able to detect the RV signals K_i for Kepler-20d, K00070.04, or K00070.05, but by including these parameters, we include any inflation these may imply for the uncertainties on the mass estimates of Kepler-20b and Kepler-20c, and the upper limit on the mass of Kepler-20d.)

We computed each transit shape using the analytic formulae of Mandel & Agol (2002). We adopted a fourth-order nonlinear limb-darkening law with coefficients fixed to those presented by Claret & Bloemen (2011) for the *Kepler* bandpass using the parameters $T_{\rm eff}$, $\log g$, and [Fe/H] determined from spectroscopy (Section 3.3). Our approach implicitly assumes that all five transit signals are due to planets orbiting Kepler-20; the validation of the three largest planets, Kepler-20b, Kepler-20c, and Kepler-20d, is presented in Section 4. Using the validation approach presented in Section 4, we are not able to validate the remaining two candidates K00070.04 and K00070.05. Instead, this difficult problem is deferred to a subsequent study (Fressin et al. 2012b). We further assumed that the planets followed non-interacting Keplerian orbits, and that the eccentricity of each planetary orbit was constrained to be less than the value at which it would cross the orbit of another planet, $e \leqslant 0.396$ (Kepler-20b), 0.319 (Kepler-20c), 0.601 (Kepler-20d), 0.283 (K00070.04), and 0.325 (K00070.05). Finally, we included an additional error term on the radial velocities (beyond those appearing in Table 5) with a typical amplitude of 2 m s^{-1}, to assure that we were not underestimating the uncertainties on the radial velocities (and hence the planetary masses).

[19] http://archive.stsci.edu/kepler

We included a prior on $\rho_\star$ as follows. We matched the spectroscopically estimated $T_{\rm eff}$, $\log g$, and [Fe/H] and the corresponding error estimates (see Section 3.3) to the Yonsei–Yale evolution tracks (Yi et al. 2001; Demarque et al. 2004) with a Markov Chain Monte Carlo (MCMC) routine to produce posterior distributions of stellar mass $M_\star$ and stellar radius $R_\star$, which in turn we used to generate the prior on $\rho_\star$ used for the determination of the best-fit model. The posterior distributions of $(a/R_\star)_i$ were obtained by calculating $(a/R_\star)_i$ for each element of the Markov Chain.

We identified the best-fit model by minimizing the χ^2 statistic using a Levenberg–Marquardt algorithm. We estimated the uncertainties via the construction of a co-variance matrix (these results were also used below in the estimate of the width of the Gibbs sample for our MCMC analysis). We then adopted the best-fit model (and its estimated uncertainties) as the seed for an MCMC analysis to determine the posterior distributions of all the model parameters. We used a Gibbs sampler to identify new jump values of test parameter chains by drawing from a normal distribution. The width of the normal distribution for each fitted parameter was initially determined by the error estimates from the best-fit model. We generated 500 elements in the chain and then stopped to examine the success rate, and then we scaled the normal distributions using Equation (8) from Gregory (2011). We repeated this process until the success rate for each parameter fell between 22% and 28%. We then held the width of the normal distribution fixed.

To handle the large correlation between the model parameters, we adopted a hybrid MCMC algorithm based on Section 3 of Gregory (2011). The routine works by randomly using a Gibbs sampler or a buffer of previously computed chain points to generate proposals for a jump to a new location in the parameter space in a manner similar to the DE-MC algorithm (Ter Brakk 2006). The addition of the buffer allows for a calculation of vectorized jumps, which permits efficient sampling of highly correlated parameter space. Once the proposals drawn from the buffer reached an acceptance rate that fell between 22% and 28%, we held the buffer fixed. With the widths of the Gibbs sampler and buffer contents stabilized, we generated four chains, each with 1,000,000 elements. The generation of four separate chains permitted us to test for convergence via a Gelman–Rubin test.

We adopted the median of the posterior distribution of each parameter as our estimate of its value, and we assigned the uncertainties by identifying the adjacent ranges of each parameter that encompassed 34% of the values above and below the median. We estimated the parameter distributions for the planetary masses and radii by combining the stellar mass and radius distributions from the evolution track fits with the model parameter distributions. The parameter estimates for the star are listed in Table 1, and the parameter estimates for the confirmed planets Kepler-20b, Kepler-20c, and Kepler-20d are listed in Table 2. The light curves phased to the times of transit of each planet or candidate are shown in Figure 2. In Figure 3, we show the radial velocities phased to the orbital periods of Kepler-20b and Kepler-20c.

We note that the values of $a/R_\star$ for K00070.04 and K00070.05 were misstated in Table 1 of Fressin et al. (2012b). The correct values are $14.4^{+1.4}_{-1.2}$ and $31.3^{+3.0}_{-2.5}$, respectively. The values of the stellar parameters were also stated incorrectly in the same table and should read $T_{\rm eff} = 5455 \pm 100$ K, $\log g = 4.4 \pm 0.1$, [Fe/H] $= +0.01 \pm 0.04$, $v \sin i < 2$ km s^{-1}, and $L/L_\odot = 0.71^{+0.14}_{-0.29}$. These changes have no effect on the conclusions of Fressin et al. (2012b).

Table 1
Parameters for the Star Kepler-20

Parameter	Value	Notes
Right Ascension (J2000)	$19^{\rm h}10^{\rm m}47\overset{\rm s}{.}52$	
Declination (J2000)	$+42^\circ 20' 19\overset{''}{.}4$	
Kepler magnitude	12.498	
r magnitude	12.423	
Spectroscopically determined parameters		
Effective temperature $T_{\rm eff}$ (K)	5455 ± 100	A
Spectroscopic gravity $\log g$ (cgs)	4.4 ± 0.1	A
Metallicity [Fe/H]	0.01 ± 0.04	A
Mt. Wilson S-value	0.183 ± 0.005	A
$\log R'_{\rm HK}$	-4.93 ± 0.05	A
Projected rotation $v \sin i$ (km s^{-1})	<2	A
Mean radial velocity (km s^{-1})	-21.87 ± 0.96	A
Radial velocity instrumental zero point γ (m s^{-1})	$-3.54^{+0.68}_{-1.02}$	B
Derived stellar properties		
Mass $M_\star$ ($M_\odot$)	0.912 ± 0.034	C
Radius $R_\star$ ($R_\odot$)	$0.944^{+0.060}_{-0.095}$	C
Density $\rho_\star$ (cgs)	1.51 ± 0.38	C
Luminosity $L_\star$ ($L_\odot$)	$0.71^{+0.14}_{-0.29}$	C
Age (Gyr)	$8.8^{+4.7}_{-2.7}$	C
Distance (pc)	290 ± 30	C

Notes. A: based on the spectroscopic analysis (Section 3.3).
B: not a physical parameter, reported here for completeness.
C: based on a comparison of stellar evolutionary tracks to constraints from the spectroscopically determined parameters (Section 3.3) and the transit durations (Section 2.2).

2.3. Limits on Motion of Photocentroid

While the analysis above provides the parameter estimates of the five planet candidates under the assumption that each are planets orbiting Kepler-20, it does not address the concern that some or all of these five candidates result instead from an astrophysical false positive (i.e., a blend of several stars within the *Kepler* photometric aperture, containing an eclipsing component). In Section 4, we use the BLENDER method to demonstrate that this possibility is extremely unlikely for Kepler-20b, Kepler-20c, and Kepler-20d, and it is this BLENDER work that is the basis for our claim that each of these three objects is a planet. Another means to identify astrophysical false positives is to examine the *Kepler* pixel data to detect the shift in the photocentroid of the image (e.g., Batalha et al. 2010; Torres et al. 2011; Ballard et al. 2011) of Kepler-20 during times of transit, which we discuss below. Although we do not use the results presented below as part of the BLENDER work, we include a description of it here as it provides an independent argument against the hypothesis that the photometric signals result from an astrophysical false positive and not from planetary companions to Kepler-20.

We use two methods to examine the *Kepler* pixel data to evaluate the location of the photocenter and thus to search for astrophysical false positives: (1) the direct measurement of the source location via difference images, the pixel response function (PRF) centroid method, and (2) the inference of the source location from photocenter motion associated with the transits, the flux-weighted centroid method. In principle both techniques are similarly accurate, but in practice the flux-weighted centroid technique is more sensitive to noise for low signal-to-noise ratio (S/N) transits. We use both techniques because they are both subject to biases due to various systematics but respond to those systematics in different ways.

Table 2
Physical and Orbital Parameters for Kepler-20b, Kepler-20c, and Kepler-20d

Parameter	Kepler-20b	Kepler-20c	Kepler-20d	Notes
Orbital period P (days)	$3.6961219^{+0.0000043}_{-0.0000064}$	10.854092 ± 0.000013	$77.61184^{+0.00015}_{-0.00037}$	A
Midtransit time T_0 (BJD)	$2454967.50027^{+0.00058}_{-0.00068}$	$2454971.60758 \pm 0.00046$	$2454997.7271^{+0.0016}_{-0.0019}$	A
Scaled semimajor axis $a/R_\star$	$10.29^{+0.97}_{-0.83}$	$21.1^{+2.0}_{-1.7}$	$78.3^{+7.4}_{-6.3}$	A
Scaled planet radius $R_p/R_\star$	$0.01855^{+0.00026}_{-0.00031}$	0.02975 ± 0.00032	$0.02670^{+0.00046}_{-0.00069}$	A
Impact parameter b	$0.633^{+0.025}_{-0.021}$	$0.594^{+0.018}_{-0.021}$	$0.588^{+0.041}_{-0.032}$	A
$e\cos(\omega)$	$-0.004^{+0.033}_{-0.055}$	$-0.097^{+0.054}_{-0.072}$	$-0.002^{+0.025}_{-0.045}$	A
$e\sin(\omega)$	$-0.021^{+0.021}_{-0.030}$	$-0.011^{+0.031}_{-0.022}$	$-0.007^{+0.025}_{-0.022}$	A
Orbital inclination i (deg)	$86.50^{+0.36}_{-0.31}$	$88.39^{+0.16}_{-0.14}$	$89.570^{+0.043}_{-0.048}$	A
Orbital eccentricity e	<0.32	<0.40	<0.60	A
Orbital semi-amplitude K ($m\,s^{-1}$)	$3.72^{+0.76}_{-1.09}$	$4.83^{+1.03}_{-0.98}$	$1.2^{+1.0}_{-1.3}$	A
Mass M_p ($M_\oplus$)	$8.7^{+2.1}_{-2.2}$	$16.1^{+3.3}_{-3.7}$	$<20.1(2\sigma)$	B
Radius R_p ($R_\oplus$)	$1.91^{+0.12}_{-0.21}$	$3.07^{+0.20}_{-0.31}$	$2.75^{+0.17}_{-0.30}$	B
Density ρ_p ($g\,cm^{-3}$)	$6.5^{+2.0}_{-2.7}$	$2.91^{+0.85}_{-1.08}$	<4.07	B
Orbital semimajor axis a (AU)	$0.04537^{+0.00054}_{-0.00060}$	0.0930 ± 0.0011	$0.3453^{+0.0041}_{-0.0046}$	B
Equilibrium temperature $T_{\rm eq}$ (K)	1014	713	369	C

Notes. A: based on the joint modeling (Section 2.2) of the light curve and radial velocities, with eccentricities constrained to avoid orbit crossing.
B: based on the results from A and estimates of $M_\star$ and/or $R_\star$ from Table 1.
C: calculated assuming a Bond albedo of 0.5 and isotropic re-radiation of absorbed flux from the entire planetary surface.

Table 3
Offsets between Photocenter of Transit Signal and Kepler-20

Candidate	PRF Centroid (arcsec)	Significance[a]	Flux-weighted Centroid (arcsec)	Significance[a]
Kepler-20b	0.071 ± 0.25	0.29	0.41 ± 0.24	1.72
Kepler-20c	0.021 ± 0.17	0.12	0.072 ± 0.22	0.32
Kepler-20d	0.69 ± 0.74	0.92	3.07 ± 1.96	1.59
K00070.04	0.24 ± 0.51	0.47	2.14 ± 1.79	1.20
K00070.05	0.73 ± 0.45	1.62	1.76 ± 1.91	0.93

Note. [a] Offset/uncertainty.

In our difference image analysis (Torres et al. 2011), we evaluate the difference between average in-transit pixel images and average out-of-transit images. In the absence of pixel-level systematics, the pixels with the highest flux in the difference image will form a star image at the location of the transiting object, with amplitude equal to the depth of the transit. A fit of the *Kepler* PRF (Bryson et al. 2010) to both the difference and out-of-transit images provides the offset of the transit source from Kepler-20. We measure difference images separately in each quarter and estimate the transit source location as the robust uncertainty-weighted average of the quarterly results.

We measure photocenter motion by computing the flux-weighted centroid of all pixels downlinked for Kepler-20, generating a centroid time series for row and column. We fit the modeled transit to the whitened centroid time series transformed into sky coordinates. We perform a fit for each quarter and infer the source location by scaling the difference of these two centroids by the inverse of the flux as described in Jenkins et al. (2010a).

Both the difference image and photocenter motion methods are vulnerable to various systematics, which may bias the result. The PRF fit to the difference and out-of-transit pixel images is biased by PRF errors described in Bryson et al. (2010). The photocenter technique is biased by stars not being completely captured by the available pixels. These types of biases will vary from quarter to quarter. Both methods are vulnerable to crowding, depending on which pixels are downlinked, which varies from quarter to quarter. We ameliorate these biases by taking the uncertainty-weighted robust average of the source locations over available quarters. Because the biases of these difference image and photocenter motion techniques differ, we take agreement of the multi-quarter averages as evidence that we have faithfully measured the source location of the transit signal.

Table 3 provides the offsets of the transit signal source from Kepler-20 averaged over Q1−Q7 for all five planet candidates. The quarterly measurements and averages for the PRF centroid method are shown in Figure 4. All the average offsets are within 2σ of Kepler-20.

2.4. Stellar Activity and Rotation from the Kepler Light Curve

While the polynomial-fitting approach in Section 2.2 is well suited to cleaning the time series for the transit analysis, it annihilates any long-term variability, such as that due to rotationally modulated star spots. Subsequent to the analysis in Section 2.2, we obtained a version of the *Kepler* photometry from Q1−Q8 using the new pipeline `PDC-MAP` (Jenkins et al. 2011), which more effectively removes non-astrophysical systematics in the photometry while leaving the stellar variability intact. We used this `PDC-MAP` corrected light curve to evaluate the rotational period and stellar activity of the star. We computed a Lomb–Scargle periodogram and found the highest power peak at a period of 25 days, with a lobe on that peak at around 26 days.

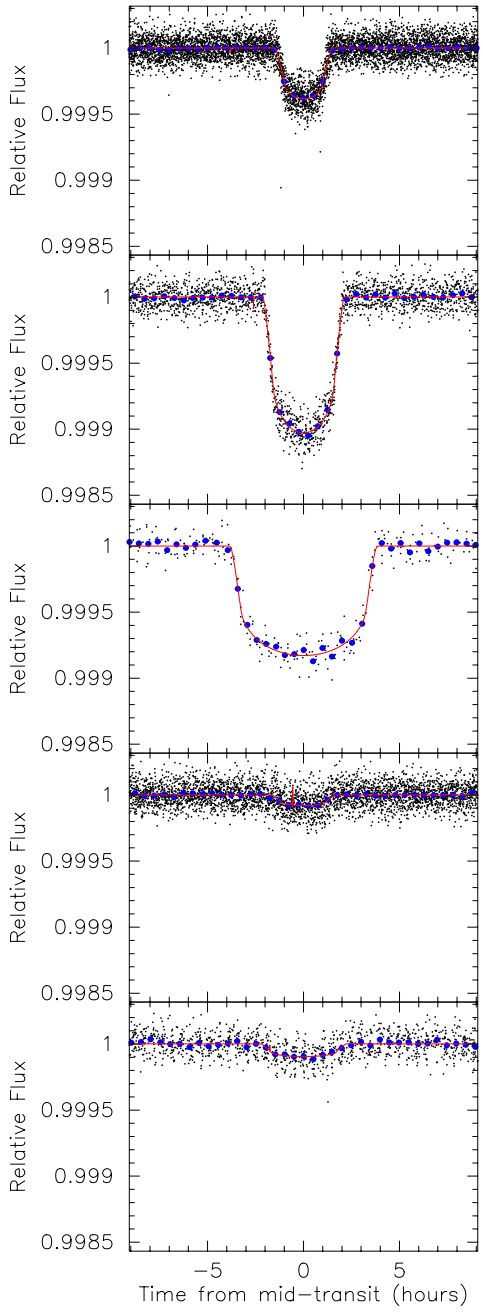

Figure 2. *Kepler* light curves with an observational cadence of 30 minutes (black points) of Kepler-20, phased to each of the periods of the five candidate transiting planets (only data in the vicinity of each phased transit are shown). Kepler-20b, 20c, 20d, K00070.04, and K00070.05 are shown from top to bottom. Blue points with error bars show these measurements binned in phase in increments of 30 minutes. The red curve shows the global best-fit model (see Section 2.2), which includes smoothing to match this 30 minute cadence.

(A color version of this figure is available in the online journal.)

This peak is also accompanied by significant power at periods between 24 and 32 days. The distribution of periodicities and in particular the lobed, broad appearance of the peak with the highest power are strongly reminiscent of the activity behavior of the Sun, where differential rotation is responsible for a range of periods from approximately 25 days at the equator to 34 days at the poles. Indeed, the amplitude of spot-related variability on Kepler-20 is very similar to that of the active Sun, as measured during the 2001 season by the *Solar and Heliospheric Observatory* (*SOHO*) Virgo instrument. Using the *SOHO* light

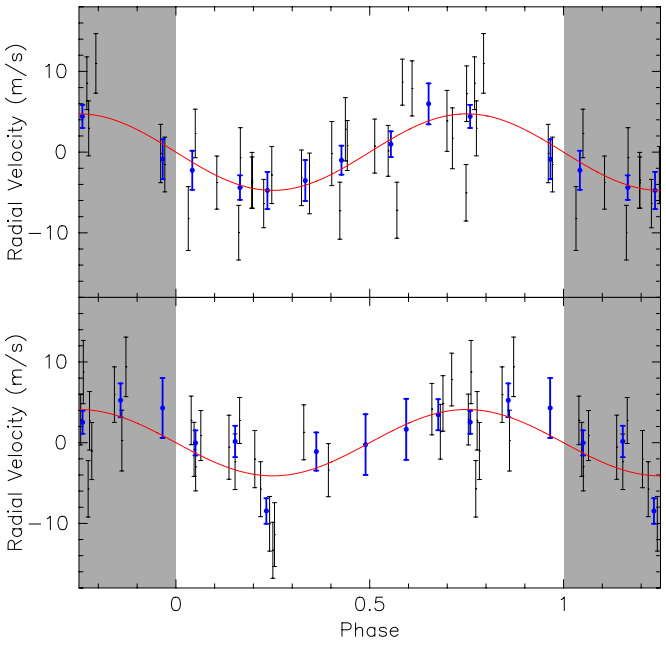

Figure 3. Upper panel: radial velocities of Kepler-20 after correcting for the best-fit amplitudes of Kepler-20b, Kepler-20d, K00070.04, and K00070.05, leaving the effect of only Kepler-20c and plotted as a function of its orbital phase of Kepler-20c. Individual measurements are shown as gray points, and these values binned in increments of 0.1 phase units are shown in blue. The phase coverage is extended by 0.25 phase units on either side to show data continuity, but it should be noted that the values in these gray regions are plotted twice. The red curve is the best-fit model for the radial velocity variation of the star after the subtraction of the effect of Kepler-20b, Kepler-20d, K00070.04, and K00070.05. Lower panel: same as above, but showing the radial velocities (in gray, with binned points in blue) and model (in red) of Kepler-20 after correcting for effect of Kepler-20c, Kepler-20d, K00070.04, and K00070.05, leaving the effect of only Kepler-20b and plotted as a function of its orbital phase.

(A color version of this figure is available in the online journal.)

curves treated to resemble *Kepler* photometry (as described in Basri et al. 2011), we compared the amplitude of variability of Kepler-20 and the active Sun; the two light curves (and the Lomb–Scargle periodogram of each) are shown in Figure 5. We found that Kepler-20 has spot modulation roughly 30% higher in amplitude than that of our Sun. Our estimate of the rotation period (above) for Kepler-20 is consistent with both its spectroscopically estimated $v \sin i < 2$ km s^{-1} and an estimate of the rotation period, 31 days, based on its Ca H and K emission $\log R'_{\rm HK}$ (see Section 3.3). Together, the period and variability indicate that Kepler-20 is very similar to (but perhaps somewhat more active than) our own star.

3. FOLLOW-UP OBSERVATIONS

3.1. High-resolution Imaging

In order to place limits on the presence of stars near the target that could be the source of one or more of the transit signals, we gathered high-resolution imaging of Kepler-20 with three separate facilities: we obtained near-infrared adaptive optics images with both the Palomar Hale 5 m telescope and the Lick Shane 3 m telescope, and we gathered optical speckle observations with the Wisconsin Indiana Yale NOAO (WIYN) 3.5 m telescope. Ultimately we used only the Palomar observations in our BLENDER analysis (Section 4) as these were the most constraining, but we describe all three sets of observations here for completeness.

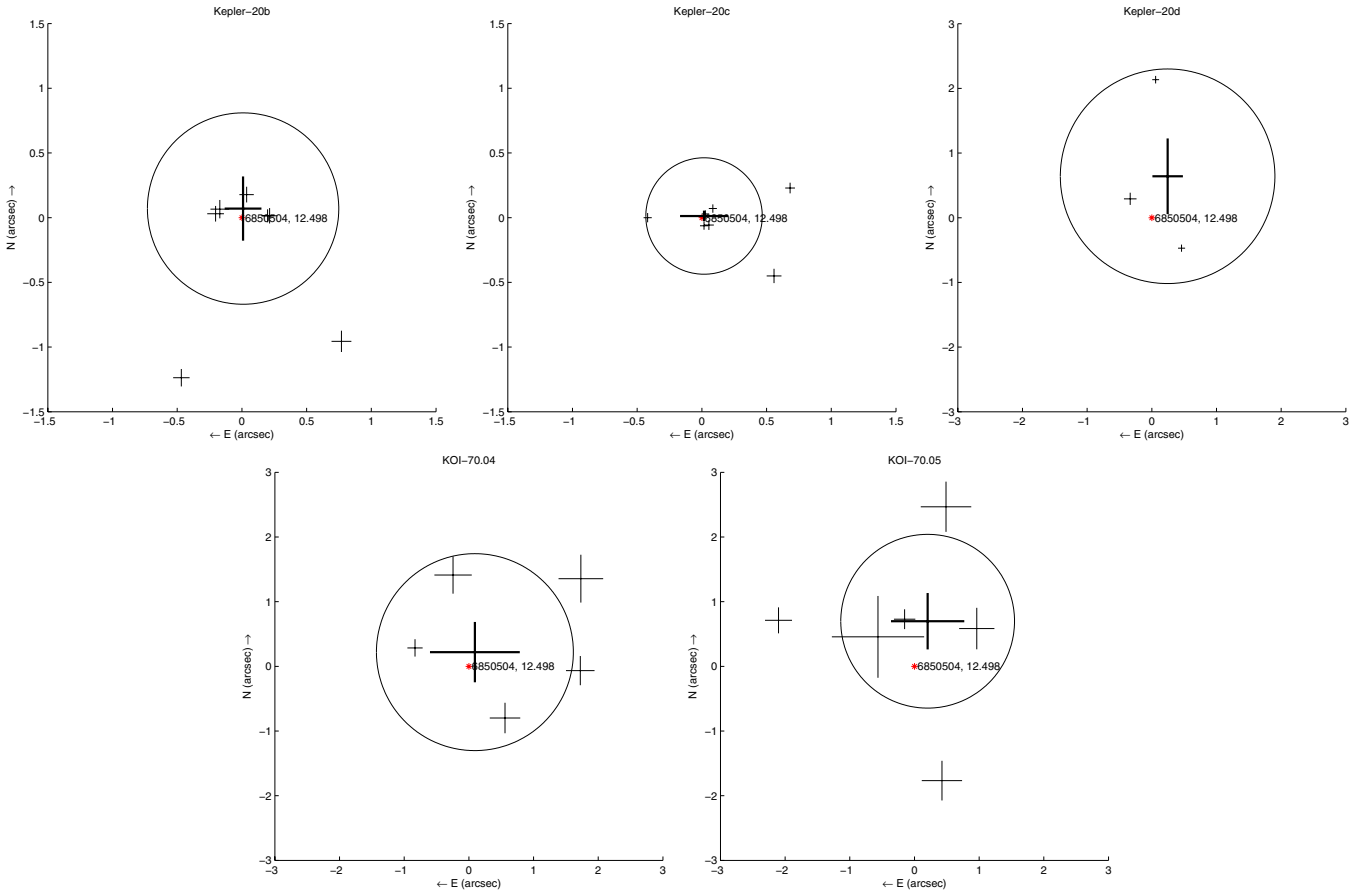

Figure 4. Quarterly and average source locations using the difference image (PRF centroid) method for Kepler-20b (top left), Kepler-20c (top center), Kepler-20d (top right), K00070.04 (bottom left), and K00070.05 (bottom right). The light crosses show the individual quarter measurements, and the heavy crosses show the uncertainty-weighted robust average. The length of the crosses shows the 1σ uncertainty of each measurement in R.A. and decl. The circles have radius 3σ and are centered at the average measured source location. The location of Kepler-20 is shown by the red asterisk and labeled with its KIC number. In all the panels, the offset between the measured source location and the target is less than 2σ.

(A color version of this figure is available in the online journal.)

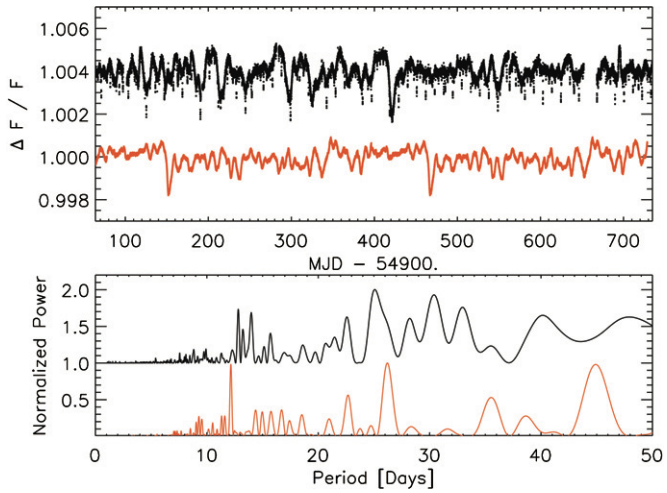

Figure 5. Upper panel: PDC-MAP corrected light curve for Kepler-20 from Q1 to Q8 (black points), showing Kepler-20's intrinsic stellar variability after the removal of instrumental effects. Orange points show the light curve for the 2001 active Sun from the *SOHO* Virgo instrument $g+r$ observations for comparison (light curve prepared as described in Basri et al. 2010). Lower panel: Lomb–Scargle periodogram for each of the two curves appearing in the upper panel.

(A color version of this figure is available in the online journal.)

3.1.1. Adaptive Optics Imaging

We obtained near-infrared adaptive optics imaging of Kepler-20 on the night of UT 2009 September 9 with the Palomar Hale 5 m telescope and the PHARO near-infrared camera (Hayward et al. 2001) behind the Palomar adaptive optics system (Troy et al. 2000). We used PHARO, a 1024×1024 HgCdTe infrared array, in 25.1 mas pixel^{-1} mode, yielding a field of view of $25''$. We gathered our observations in the J ($\lambda_0 = 1.25\,\mu$m) filter. We collected the data in a standard five-point quincunx dither pattern of $5''$ steps interlaced with an off-source ($60''$ east and west) sky dither pattern. The integration time per source was 4.2 s at J. We acquired a total of 15 frames for a total on-source integration time of 63 s. The adaptive optics system guided on the primary target itself; the FWHM of the central core of the resulting point-spread function (PSF) was $0\farcs07$.

We further obtained near-infrared adaptive optics imaging on the night of UT 2011 June 17 with the Lick Shane 3 m telescope and the IRCAL near-infrared camera (Lloyd et al. 2000) behind the natural guide star adaptive optics system. IRCAL is a 256×256 pixel PICNIC array with a plate scale of 75.6 mas pixel^{-1}, yielding a total field of view of $19\farcs6$. We gathered our observations using the K_s ($\lambda_0 = 2.145\,\mu$m) filter, and, as with the Palomar observations, we used a standard five-point dither pattern. The integration time per frame was 120 s;

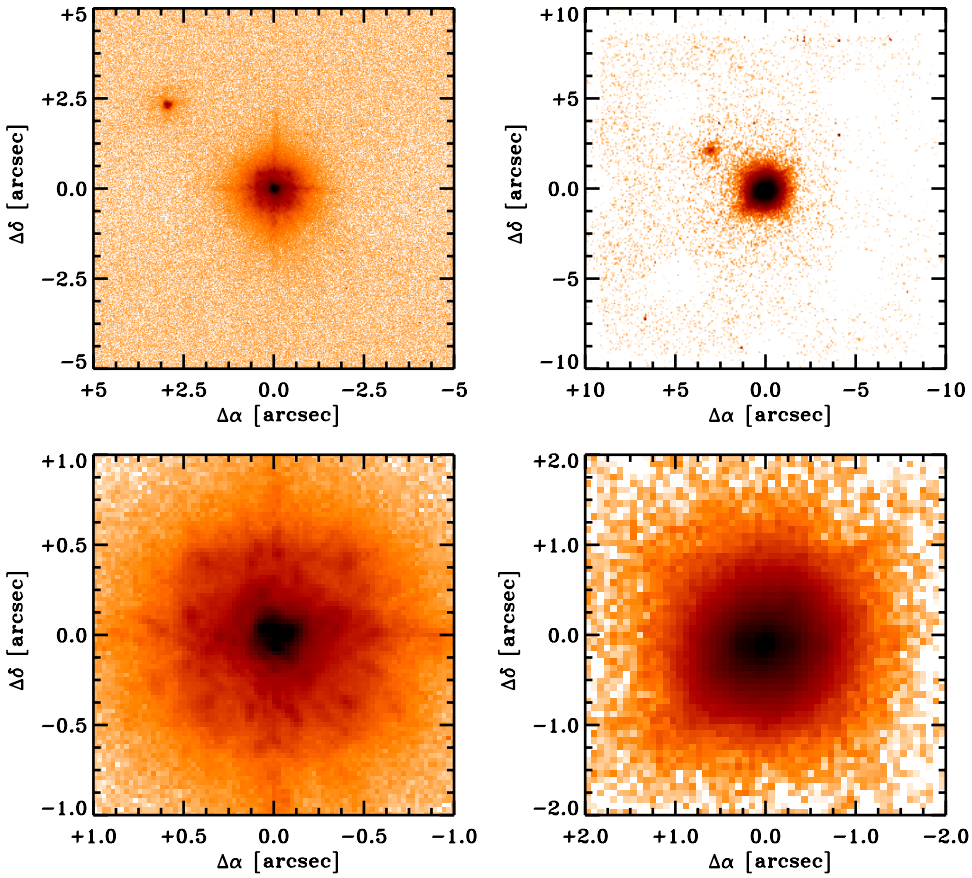

Figure 6. Palomar J (left) and Lick K_s (right) adaptive optics images of Kepler-20. The top row displays a $10'' \times 10''$ field of view for the Palomar J image and a $20'' \times 20''$ for the Lick K_s image. The bottom row displays zoomed images highlighting the area immediately around the target.
(A color version of this figure is available in the online journal.)

we acquired 10 frames for a total on-source integration time of 1200 s. The adaptive optics system guided on the primary target itself; the FWHM of the central core of the resulting PSF was 0.″79. The final co-added images at J and K_s are shown in Figure 6.

In addition to Kepler-20, we detected two additional sources. The first source is 3.″8 to the northeast of the target and is fainter by $\Delta J \approx 4.5$ mag and $\Delta K_s \approx 4.2$ mag. The star has an infrared color of $J - K_s = 0.19 \pm 0.02$ mag, which yields an expected *Kepler* magnitude of $Kp = 16.1 \pm 0.2$ mag (Howell et al. 2012). A much fainter source, at $11''$ to the southeast, was detected only in the Palomar J data and is $\Delta J = 8.5$ mag fainter than the primary target. The fainter source, based on expected stellar $Kp - J$ colors (Howell et al. 2012), has an expected *Kepler* magnitude of $Kp = 21.0 \pm 0.7$ mag.

No additional sources were detected in the imaging. We determined the sensitivity limits of the imaging by calculating the noise in concentric rings radiating out from the centroid position of the primary target, starting at one FWHM from the target with each ring stepped one FWHM from the previous ring. The 3σ limits of the J-band and K-band imaging were approximately 20 mag and 16 mag, respectively (see Figure 7). The respective J-band and K-band imaging limits are approximately 8.5 and 5.5 mag fainter than the target, corresponding to contrasts in the *Kepler* bandpass of approximately 9 mag and 6.5 mag.

3.1.2. Speckle Imaging

We obtained speckle observations of Kepler-20 at the WIYN 3.5 m telescope on two different nights, UT 2010 June 18 and UT 2010 September 17. We gathered both sets of observations with the new dual channel speckle camera described in Horch et al. (2011). On both nights the data consisted of three sets of 1000 exposures each with an individual exposure time of 40 ms, with images gathered simultaneously in two filters. The data collection, reduction, and image reconstruction process are described in the aforementioned paper as well as in Howell et al. (2011), and the latter presents details of the 2010 observing season of observations with the dual channel speckle camera for the *Kepler* follow-up program.

On both occasions our speckle imaging did not detect a companion to Kepler-20 within an annulus of 0.05–1.8 arcsec from the target. The September observation yielded detection limits of 3.82 (in V) and 3.54 (in R) mag fainter than Kepler-20. The June observation yielded limits of 3.14 and 4.92 fainter in V and R, respectively. Therefore, we rule out the presence of a second star down to 3.82 mag fainter in V and 4.92 mag fainter in R over an angular distance of 0.05–1.8 arcsec from Kepler-20.

3.2. Photometry with the Spitzer Space Telescope

An essential difference between true planetary transits and astrophysical false positives resulting from blends of stars is that the depth of a planetary transit is achromatic (neglecting the small effect of stellar limb darkening), whereas false positives are not (except in the unlikely case that the effective temperatures of the contributing stars are extremely similar). By providing infrared time series spanning times of transit, the *Warm Spitzer* Mission has assisted in the validation of many transiting planet systems, including Kepler-10 (Fressin et al.

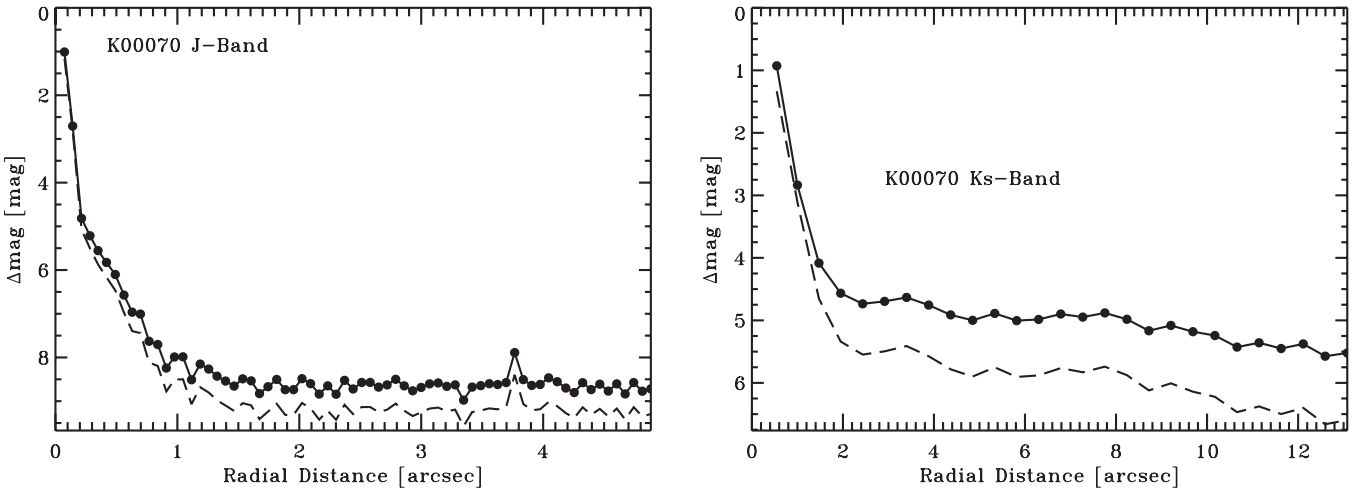

Figure 7. Left panel: the sensitivity limits of the Palomar *J*-band adaptive optics imaging are plotted as a function of radial distance from the primary target. The filled circles and solid line represent the measured *J*-band limits; each filled circle represents one step in FWHM. The dashed line represents the derived corresponding limits in the *Kepler* bandpass based on the expected $Kp - J$ colors (Howell et al. 2012). Right panel: same as above, but showing the sensitivity limits of the Lick K_s-band adaptive optics imaging. The dashed line is based on the expected $Kp - K_s$ colors.

2011), Kepler-14 (Buchhave et al. 2011), Kepler-18 (Cochran et al. 2011), Kepler-19 (Ballard et al. 2011), and CoRoT-7 (Fressin et al. 2012a). We describe below our observations and analysis of *Warm Spitzer* data spanning transits of Kepler-20c and Kepler-20d, which provide independent support of their planetary nature.

3.2.1. Observations and Extraction of the Warm Spitzer Time Series

We used the IRAC camera (Fazio et al. 2004) on board the *Spitzer Space Telescope* (Werner et al. 2004) to observe Kepler-20 spanning one transit of Kepler-20c and two transits of Kepler-20d. We gathered our observations at 4.5 μm as part of program ID 60028. The visits lasted 8.5 hr for Kepler-20c and 16.5 hr for both visits of Kepler-20d. We used the full-frame mode (256 × 256 pixels) with an exposure time of 12 s per image, which yielded 2451 and 4643 images per visit for Kepler-20c and Kepler-20d, respectively.

The method we used to produce photometric time series from the images is described in Désert et al. (2009). It consists of finding the centroid position of the stellar PSF and performing aperture photometry using a circular aperture on individual Basic Calibrated Data (BCD) images delivered by the *Spitzer* archive. These files are corrected for dark current, flat-fielding, detector nonlinearity and converted into flux units. We converted the pixel intensities to electrons using the information given in the detector gain and exposure time provided in the image headers; this facilitates the evaluation of the photometric errors. We adjusted the size of the photometric aperture to yield the smallest errors; for these data the optimal aperture was found to have a radius of 3.0 pixels. We found that the transit depths and errors varied only weakly with the aperture radius for each of the light curves. We used a sliding median filter to identify and trim outliers that differed in flux or positions by greater than 5σ. We also discarded the first half hour of observations, which are affected by a significant jitter before the telescope stabilizes. We estimated the background by fitting a Gaussian to the central region of the histogram of counts from the full array. Telescope pointing drift resulted in fluctuations of the stellar centroid position, which, in combination with intra-pixel sensitivity variations, produces systematic noise in the raw light curves. A description of this effect, known as the pixel-phase effect, is given in the *Spitzer*/IRAC data handbook (IRAC 2011) and is well known in exoplanetary studies (e.g., Charbonneau et al. 2005; Knutson et al. 2008). After correction for this effect (see below), we found that the point-to-point scatter in the light curve indicated an achieved S/N of 220 per image, corresponding to 85% of the theoretical limit.

3.2.2. Analysis of the Warm Spitzer Light Curves

We modeled the time series using a model that was a product of two functions, one describing the transit shape and the other describing the variation of the detector sensitivity with time and sub-pixel position, as described in Désert et al. (2011b). For the transit light-curve model, we used the transit routine `OCCULTNL` from Mandel & Agol (2002). This function depends on the parameters $(R_p/R_\star)_i$, $(a/R_\star)_i$, b_i, and $T_{0,i}$, where i = {Kepler-20c, Kepler-20d}, the two candidate planets for which we gathered observations. The contribution of stellar limb darkening at 4.5 μm is negligible given the low precision of our *Warm Spitzer* data, and so we neglect this effect. We allow only $(R_p/R_\star)_i$ to vary in our analysis; the other parameters are set to the values derived from the analysis of the *Kepler* light curve (see Table 2). Because of the possibility of TTVs (see Section 5), we set the values of $T_{0,i}$ to the values measured from *Kepler* for the particular event. Our model for the variation of the instrument response consists of a sum of a linear function of time and a quadratic function (with four parameters) of the x and y sub-pixel image position. We simultaneously fit the instrumental function and the transit shape for each individual visit. The errors on each photometric point were assumed to be identical and were set to the rms residuals to the initial best fit obtained.

To obtain an estimate of the correlated and systematic errors in our measurements, we use the residual permutation bootstrap method as described in Désert et al. (2009). In this method, the residuals of the initial fit are shifted systematically and sequentially by one frame and added to the transit light-curve model, which is then fit once again and the process is repeated. We assign the error bars to be the region containing 34% of the results above and 34% of the results below the median of the distributions, as described in Désert et al. (2011a). As we observed two transits of Kepler-20d, we further evaluated the

Table 4
Transit Depths at 4.5 μm from *Warm Spitzer*

Candidate	AOR Name	Date of Observation [UT]	Data Number	Time of Transit Center [BJD]	Transit Depth (%)
Kepler-20c	r41165824	2010 Dec 5	2291	2455536.0209	0.075 ± 0.015
Kepler-20d	r39437568	2010 Sep 24	4451	2455463.4022	$0.063^{+0.019}_{-0.014}$
Kepler-20d	r41164544	2010 Dec 10	4383	2455540.9925	0.067 ± 0.016
Kepler-20d	Weighted mean	...	...	...	0.065 ± 0.011

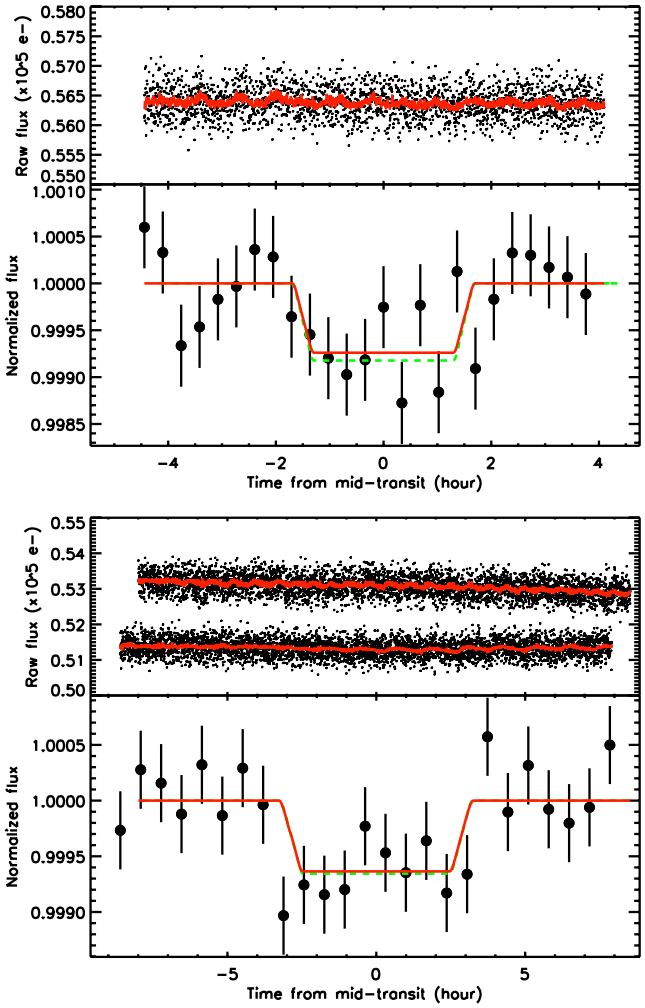

Figure 8. *Warm Spitzer* transit light curves of Kepler-20 observed in the IRAC bandpass at 4.5 μm spanning times of transit of Kepler-20c (upper half of figure) and Kepler-20d (lower half of figure). For each candidate, the raw and unbinned time series are shown in the upper panels, and the red solid lines correspond to the best-fit models, which include both the effects of the instrumental variation with time and image position and the planetary transit (see Section 3.2). In the lower panel for each candidate, we display these data after correcting for the instrumental model, normalizing, and binning by 20 minutes. In the case of Kepler-20d we co-added the two light curves. The best-fit model for the transits is plotted in red, and the transit shapes expected from the parameters estimated from the *Kepler* observations (Table 2) are overplotted as dashed green lines. The transit depths measured in the *Spitzer* and *Kepler* bandpasses agree to better than 1σ.

(A color version of this figure is available in the online journal.)

weighted mean of the transit depth for this candidate. In Table 4, we provide a summary of the *Spitzer* observations and report our estimates of the transit depths and uncertainties. In Figure 8, we plot both the raw and corrected time series for each candidate and overplot the theoretical curve expected using the parameters estimated from the *Kepler* photometry (see below).

The adaptive optics images described in Section 3.1.1 reveal the presence of a star adjacent to Kepler-20. This adjacent star is 4.5 mag fainter in J band than Kepler-20 and located at an angular separation of 3.″8, which corresponds to 3.1 IRAC pixels. We tested whether the measured transit depths have to be corrected to take into account the contribution from this stellar companion. We computed the theoretical dilution factor by extrapolating the J-band measurements to the *Spitzer* bandpass at 4.5 μm. We estimate that 1.6% of the photons recorded during the observation come from the companion star. For a blend of two sources, the polluted transit depth would be $d/(1+\epsilon)$, where d is the unblended transit depth and $\epsilon = 1.6\%$. Since the effect on d is well below our detection threshold, we conclude that the presence of the contaminant star near Kepler-20 does not affect our estimates of the transit depths.

We calculate the transit shapes that would be expected from the parameters estimated from the *Kepler* photometry (Table 2) and overplot these on the *Spitzer* time series in Figure 8. The depths we measure with *Spitzer* are in agreement with the depths expected from the *Kepler*-derived parameters at the 1σ level. Our *Spitzer* observations demonstrate that the transit signals of Kepler-20c and Kepler-20d are achromatic, as expected for planetary companions and in conflict with the expectation for most (but not all) astrophysical false positives resulting from blends of stars within the photometric aperture of *Kepler*.

3.3. Spectroscopy

We obtained 30 high-resolution spectra of Kepler-20 between UT 2009 August 30 and 2011 June 16 using the HIRES spectrometer on the Keck I 10 m telescope (Vogt et al. 1994). We took spectra with the same spectrometer setup of HIRES, and with the same spectroscopic analysis, that we normally use for precise Doppler work of nearby FGK stars (Johnson et al. 2011), which typically yields a Doppler precision of 1.5 m s^{-1} for slowly rotating FGKM stars. Typical exposure times ranged from 30 to 45 minutes, yielding an S/N of 120 pixel^{-1} (1.3 km s^{-1}). The first nine observations were made with the B5 decker (0.″87 × 3.″0) that does not permit moonlight subtraction. The remaining 21 observations were made with the C2 decker (0.″87 × 14.″0) that permits sky subtraction. The internal errors were estimated to be between 1.5 and 2 m s^{-1}. We augmented these uncertainties by adding a jitter term of 2.0 m s^{-1} in quadrature. The earlier nine observations are vulnerable to modest contamination from moonlight, and we have further augmented the uncertainties for these nine values by adding in quadrature a term of 2.7 m s^{-1}, which is based on the ensemble performance of stars similarly affected for this magnitude. The final uncertainties range from 2.5 to 4 m s^{-1}. The estimated RVs and uncertainties are given in Table 5. We also undertook a study of these spectra to determine the spectral line bisectors with the goal of placing limits on these sufficient to preclude astrophysical false positives. However, we found that the scatter in the bisector centers was somewhat larger than

Table 5
Keck HIRES Radial Velocity Measurements for Kepler-20

Date of Obs. [BJD]	Radial Velocity ($m\,s^{-1}$)	Uncertainty[a] ($m\,s^{-1}$)
2455073.885713	−5.86	3.78
2455074.861139	−2.94	3.74
2455075.906678	1.09	3.75
2455076.883792	2.57	3.84
2455077.907884	11.08	3.82
2455081.952637	−1.51	3.83
2455082.832587	−9.53	3.78
2455083.888144	−7.17	3.84
2455084.893633	4.59	3.88
2455134.766132	−14.15	3.88
2455314.027873	2.05	2.54
2455320.085390	−9.47	2.59
2455321.072318	−4.55	2.56
2455345.011208	−8.71	2.82
2455351.073218	0.41	2.70
2455352.043110	−1.84	2.50
2455372.898433	1.71	2.62
2455374.967141	−16.20	2.62
2455378.007402	−2.59	2.53
2455380.950103	−0.62	2.55
2455403.055761	7.59	2.96
2455407.903131	−10.15	2.64
2455411.959424	−13.79	2.65
2455413.894286	−2.60	2.59
2455433.818795	4.81	2.46
2455435.841063	10.04	2.58
2455440.792117	−10.94	2.50
2455500.817440	−2.94	3.34
2455522.725846	−6.56	2.63
2455724.055721	−2.35	2.64

Note. [a] Includes jitter of 2 $m\,s^{-1}$.

the RV variations, rendering the RV detection, while sufficient for mass constraint, inconclusive for confirmation. We therefore undertook the statistical study described in Section 4.

We obtained two additional spectra of Kepler-20 with HIRES on UT 2009 September 8 and 2010 August 24. These observations were gathered without the iodine cell, so that the extracted stellar spectrum could be used for the template for the RV analysis and for estimating stellar parameters. The exposure time for the first spectrum was 30 minutes, yielding a typical S/N of 90, and the B1 decker ($R = 60{,}000$) was used. The observing conditions were slightly better when the second spectrum was obtained and a 1 hr exposure yielded an S/N of 140. The taller B3 decker ($R = 60{,}000$) was used to carry out a better sky subtraction. We analyzed these two spectra using the LTE spectral synthesis analysis software *Spectroscopy Made Easy* (SME; Valenti & Piskunov 1996; Valenti & Fischer 2005) to estimate the values of $T_{\rm eff}$, $\log g$, [Fe/H], and $v \sin i$. We found that the estimates from each spectrum were consistent to within 1σ, and hence we averaged our two estimates to obtain $T_{\rm eff} = 5455 \pm 44$ K, $\log g = 4.4 \pm 0.1$, [Fe/H] $= 0.01 \pm 0.04$, and $v \sin i < 2 {\rm km\,s^{-1}}$; the errors listed are those resulting from the analysis of each individual spectrum, and we have refrained from assuming a decrease by a factor of $\sqrt{2}$. We also proceeded to measure the flux in the cores of the Ca II H and K lines to evaluate the chromospheric activity. We measured that the ratio of emission in these lines to the bolometric emission was $\log R'_{\rm HK} = -4.93 \pm 0.05$. This estimate was derived from a Mt. Wilson-style S-value of 0.183 ± 0.005 (Isaacson & Fischer 2010), using the measured color $B - V = 0.725$. The $\log R'_{\rm HK}$ value suggests a low activity level for a star of this spectral type, which is consistent with the measured $v \sin i < 2\,{\rm km\,s^{-1}}$. Using the relations of Noyes et al. (1984) and Mamajek & Hillenbrand (2008), we infer a rotation period of 31 days.

We also gathered three moderate-S/N, high-resolution spectra of Kepler-20 for reconnaissance purposes, two with the FIbre-fed Échelle Spectrograph (FIES) at the 2.5 m Nordic Optical Telescope at La Palma, Spain (Djupvik & Andersen 2010), and one with the Tull Coudé Spectrograph on the McDonald observatory 2.7 m Harlan Smith Telescope. The FIES spectra were taken on 2009 August 5 and 6 using the medium- and high-resolution fibers, resulting in a resolution of 46,000 and 67,000, respectively. Each spectrum has a wavelength coverage of approximately 360–740 nm. The McDonald spectrum was taken on 2010 October 25, with a spectral resolution of 60,000. This spectrum was exposed to an S/N of 55 per resolution element for the specific purpose of deriving reliable atmospheric parameters for the star.

As an independent check on the parameters derived from the SME analysis of the Keck/HIRES data described above, we derived stellar parameters following Torres et al. (2002) and Buchhave et al. (2010). As part of this analysis, we employed a new fitting scheme that is currently under development by L. Buchhave, allowing us to extract precise stellar parameters from the spectra. We analyzed the two FIES spectra, the McDonald spectrum, and the three HIRES template spectra. These results were found to be consistent within the errors. Taking the average of the stellar parameters from the different instruments yielded the following parameter estimates: $T_{\rm eff} = 5563 \pm 50$ K, $\log g = 4.52 \pm 0.10$, [m/H] $= +0.04 \pm 0.08$, and $v \sin i = 1.80 \pm 0.50\ {\rm km\,s^{-1}}$, in agreement with the parameters from SME within the uncertainties. The average systemic RV of the six observations was $-21.87 \pm 0.96\ {\rm km\,s^{-1}}$ on the IAU standard scale, which includes the correction for the gravitational redshift of the Sun.

We note that the two analyses yielded consistent results for $\log g$, metallicity, and $v \sin i$, but that the estimates of $T_{\rm eff}$ differed by twice the formal error. Hence, we elected to adopt the results of the SME analysis for our final values, but we increased the uncertainty on $T_{\rm eff}$ to 100 K to reflect the difference between the two estimates. We list our estimates for the spectroscopically determined parameters in Table 1.

4. VALIDATION OF THE PLANETS Kepler-20b, Kepler-20c, AND Kepler-20d

While the analysis of the RV (Section 3.3) data yielded detections for Kepler-20b and Kepler-20c, we found that our analyses of the bisector spans were not sufficient to confirm the planetary origin of those variations. Moreover, for Kepler-20d, K00070.04, and K00070.05, there is no Doppler detection. We therefore rely on a fundamentally different technique to establish which, if any, of these signals can be persuasively attributed to planets. As explained in Lissauer et al. (2011a), when dynamical confirmation of a planet candidate by the RV method or by TTVs cannot be achieved, we attempt instead to validate the candidate by tabulating all viable false positives (blends) that could mimic the signal. We then assess the likelihood of these blends and compare it with an a priori estimate of the likelihood that the signal is due to a true planet. We consider the signal to be validated when the likelihood of a planet exceeds that of a false positive by a sufficiently large ratio, typically at least 300 (i.e., 3σ).

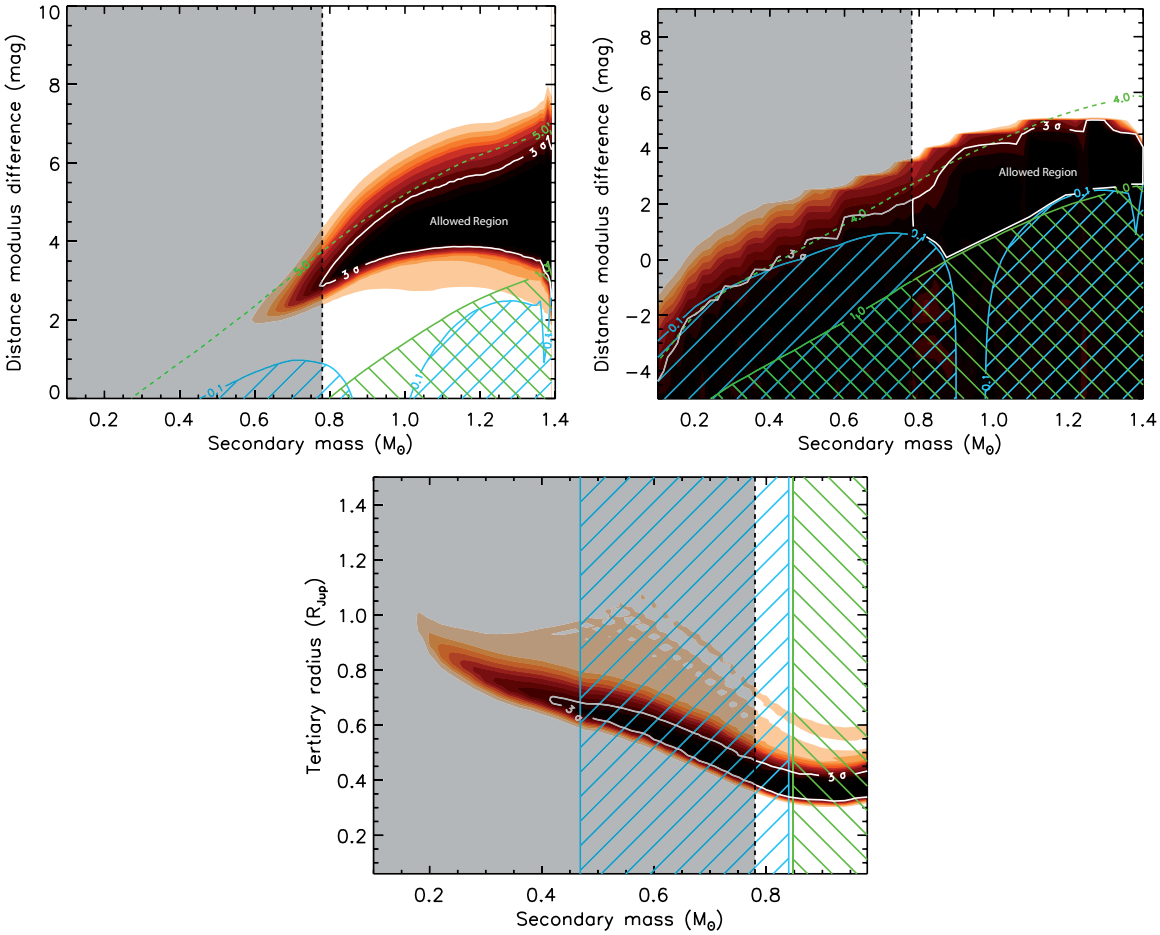

Figure 9. BLENDER goodness-of-fit contours corresponding to three different blend scenarios for Kepler-20d: background EBs (top left), background or foreground stars transited by a larger planet (top right), and stars physically associated with the target that are transited by a larger planet (bottom). The mass of the intruding star (referred to in the BLENDER nomenclature as the secondary) is shown along the horizontal axis, and the distance between this star and the target is shown on the vertical axis of the top two panels, expressed for convenience in terms of the distance modulus difference. The vertical axis in the bottom panel shows the sizes of the planets (tertiaries) orbiting physically associated stars. Viable blend models are those giving fits with χ^2 values within 3σ of the best planet fit and lie inside the white contours. Other colored areas outside the white contours indicate regions of parameter space with increasingly worse fits to the data. Blends excluded by our *Spitzer* constraints are shown with the shaded gray area (secondary masses $< 0.78\ M_{\odot}$). Blue cross-hatched areas indicate regions in which blends are excluded because they are either too red (left) or too blue (right) compared to the measured $r - K_s$ color of Kepler-20. Blend scenarios in the green cross-hatched areas are also ruled out because they are within $\Delta Kp = 1.0$ of the brightness of the target and would have been detected spectroscopically. The dashed diagonal green lines in the top panels mark the faintest blends that give acceptable fits to the light curve, corresponding to $\Delta Kp \approx 5$ in the top left panel and $\Delta Kp \approx 4$ in the top right panel. As a result of the combined constraints from our *Spitzer* observations, color index, and brightness, *all* physically associated triples are excluded.

(A color version of this figure is available in the online journal.)

Our tabulation of the viable scenarios resulting from blends was accomplished with the BLENDER algorithm (Torres et al. 2004, 2011; Fressin et al. 2011, 2012a) combined with some of the follow-up observations described earlier (high-resolution imaging, centroid motion analysis, spectroscopy, and *Spitzer* observations). BLENDER attempts to fit the *Kepler* photometry with a vast array of synthetic light curves generated from blend configurations consisting of chance alignments with background or foreground eclipsing binaries (EBs), as well as EBs physically associated with Kepler-20 (hierarchical triples). We also considered cases in which the second star is eclipsed by a larger planet, rather than by another star. A wide range of parameters is explored for the eclipsing pair, as well as for the relative distance separating it from the target. Scenarios giving poor fits to the data (specifically, a χ^2 value that indicates a discrepancy of at least 3σ worse than that corresponding to the transiting planet model) are considered to be ruled out. For full details of this technique we refer the reader to the above sources.

The combination of the shorter periods and deeper transits for Kepler-20b and Kepler-20c results in higher S/N for those signals compared to the others. Consequently, the shape of the transit is better defined, and this information makes it easier to reject false positives with BLENDER, as we show below. The transit depths of K00070.04 and K00070.05 are only 82 and 101 parts per million; this renders these signals far more challenging to validate, and we find below that we are currently not able to demonstrate unambiguously that these two signals are planetary in origin. Kepler-20d is similar in depth to Kepler-20b, but due to its longer orbital period, far fewer transits have been observed. This results in a lower S/N in the phase light curve. We begin by describing this case.

Figure 9 illustrates the BLENDER results for Kepler-20d. The three panels represent cuts through the space of parameters for blends consisting of background EBs, background or foreground stars transited by larger planets, and physically associated triples. In the latter case we find that the only scenarios able to mimic the signal are those in which the companion

Table 6
Blend Frequency Estimate for Kepler-20d (K00070.03)

		Blends Involving Stellar Tertiaries				Blends Involving Planetary Tertiaries			
Kp Range (mag) (1)	ΔKp (mag) (2)	Stellar Density[a] (per sq. deg) (3)	ρ_{max} ($''$) (4)	Stars ($\times 10^{-6}$) (5)	EBs $f_{EB} = 0.78\%$ (6)	Stellar Density[a] (per sq. deg) (7)	ρ_{max} ($''$) (8)	Stars ($\times 10^{-6}$) (9)	Blends ($\times 10^{-6}$) $R_p \in [0.4-2.0\ R_{Jup}]$, $f_{Plan} = 0.18\%$ (10)
12.5–13.0	0.5	...	...	...	...	...	...	...	...
13.0–13.5	1.0	...	...	...	...	...	...	...	...
13.5–14.0	1.5	28	0.075	0.038	0.0003	273	0.075	0.372	0.0007
14.0–14.5	2.0	77	0.093	0.164	0.0013	423	0.093	0.901	0.0016
14.5–15.0	2.5	119	0.11	0.349	0.0028	572	0.11	1.678	0.0024
15.0–15.5	3.0	238	0.13	0.975	0.0077	897	0.13	3.675	0.0053
15.5–16.0	3.5	532	0.15	2.902	0.0229	1183	0.15	6.452	0.0093
16.0–16.5	4.0	1321	0.20	12.81	0.1012	1675	0.20	16.24	0.0234
16.5–17.0	4.5	1593	0.25	24.13	0.1907	...	...	...	...
17.0–17.5	5.0	1295	0.30	28.25	0.2232	...	...	...	...
17.5–18.0	5.5	...	...	...	...	...	...	...	...
18.5–19.0	6.0	...	...	...	...	...	...	...	...
19.0–19.5	6.5	...	...	...	...	...	...	...	...
19.5–20.0	7.0	...	...	...	...	...	...	...	...
20.0–20.5	7.5	...	...	...	...	...	...	...	...
20.5–21.0	8.0	...	...	...	...	...	...	...	...
Totals		5203	...	69.62	**0.5511**	5023	...	29.32	**0.0526**

Blend frequency (BF) = $(0.5511 + 0.0526) \times 10^{-6} \approx 6.04 \times 10^{-7}$

Notes. Magnitude bins with no entries correspond to brightness ranges in which all blends are ruled out by a combination of BLENDER and other constraints.
[a] The number densities in Columns 3 and 7 differ because of the different secondary mass ranges permitted by BLENDER for the two kinds of blend scenarios, as shown in the top two panels of Figures 9.

star is orbited by a larger planet, rather than another star. The orange–red–brown–black shaded regions correspond to different levels of the χ^2 difference between blend models and the best transiting planet fit to the *Kepler* data, expressed in terms of the statistical significance of the difference (σ). The 3σ level is represented by the white contour, and only blends inside it ($<3\sigma$) are considered to give acceptable fits to the *Kepler* photometry. Other constraints further restrict the area allowed for blends. The green hatched areas are excluded because the EB is within 1 mag of the target in the Kp band and would generally have been noticed in our spectroscopic observations. The blue hatched areas are also excluded because the overall color of the blend is either too red (left in the top two panels) or too blue (right) compared to the measured Sloan–Two Micron All Sky Survey $r - K_s$ color of Kepler-20, as listed in the KIC (Brown et al. 2011). Additionally, *Spitzer* observations rule out blends involving EBs (or star+planet pairs) with stars less massive than about 0.78 $M_\odot$ (gray shaded area to the left of the vertical dotted line), because the predicted depth of the transits in the 4.5 μm bandpass of *Warm Spitzer* would be more than 3σ larger than our *Spitzer* observations indicate. Note that the combination of these constraints rules out *all* physically associated triple configurations for Kepler-20d, so that only certain blend scenarios involving background EBs or background/foreground stars transited by larger planets present suitable alternatives to a true planet model.

We estimate the frequency of these remaining blends following Torres et al. (2011) and Fressin et al. (2011), as the product of three factors: the expected number density of stars in the vicinity of Kepler-20, the area around the target within which we would miss such stars, and an estimate of how often we expect those stars to be in EBs or be transited by a larger planet of the right characteristics (specified by the stellar masses, planetary sizes, orbital eccentricities, and other characteristics as tabulated by BLENDER). For the number densities we appeal to the Besançon Galactic structure model of Robin et al. (2003). Constraints from our high-resolution imaging (see Section 3.1.1) allow us to estimate the maximum angular separation (ρ_{max}) at which blended stars would be undetected, as a function of brightness. We derive our estimates of the frequencies of EBs and larger transiting planets involved in blends from recent studies by the *Kepler* Team (Slawson et al. 2011; Borucki et al. 2011), in the same way as done for our earlier studies of Kepler-9d, Kepler-10c, and Kepler-11g (see Torres et al. 2011; Fressin et al. 2011; Lissauer et al. 2011a).

The results of our calculations for Kepler-20d, performed in half-magnitude bins, are shown in Table 6 separately for background EBs and for background or foreground stars transited by a larger planet. The first two columns give the Kp magnitude range of each bin and the magnitude difference ΔKp relative to the target, calculated at the faint end of each bin. Column 3 reports the stellar density near the target, subject to the mass constraints from BLENDER as shown in Figure 9. Column 4 gives the maximum angular separation at which background stars would escape detection in our imaging observations. In this particular case those observations are more constraining than the 3σ exclusion limit set by our analysis of the flux centroids ($0\farcs65$; see Section 3.1.1). The product of the area implied by ρ_{max} and the densities in the previous column is listed in Column 5, in units of 10^{-6}. Column 6 is the result of multiplying this number of stars by the frequency of suitable EBs ($f_{EB} = 0.78\%$; see Fressin et al. 2011). A similar calculation is performed for blends involving stars transited by larger planets and is presented in Columns 7–10, using $f_{planet} = 0.18\%$. The latter is the frequency of planets in the radius range allowed by BLENDER for these types of scenarios, which is 0.4–2.0 R_{Jup} (see Borucki et al. 2011). The sum of the contributions in each bin is given at the bottom of Columns 6 and 10. The total number of

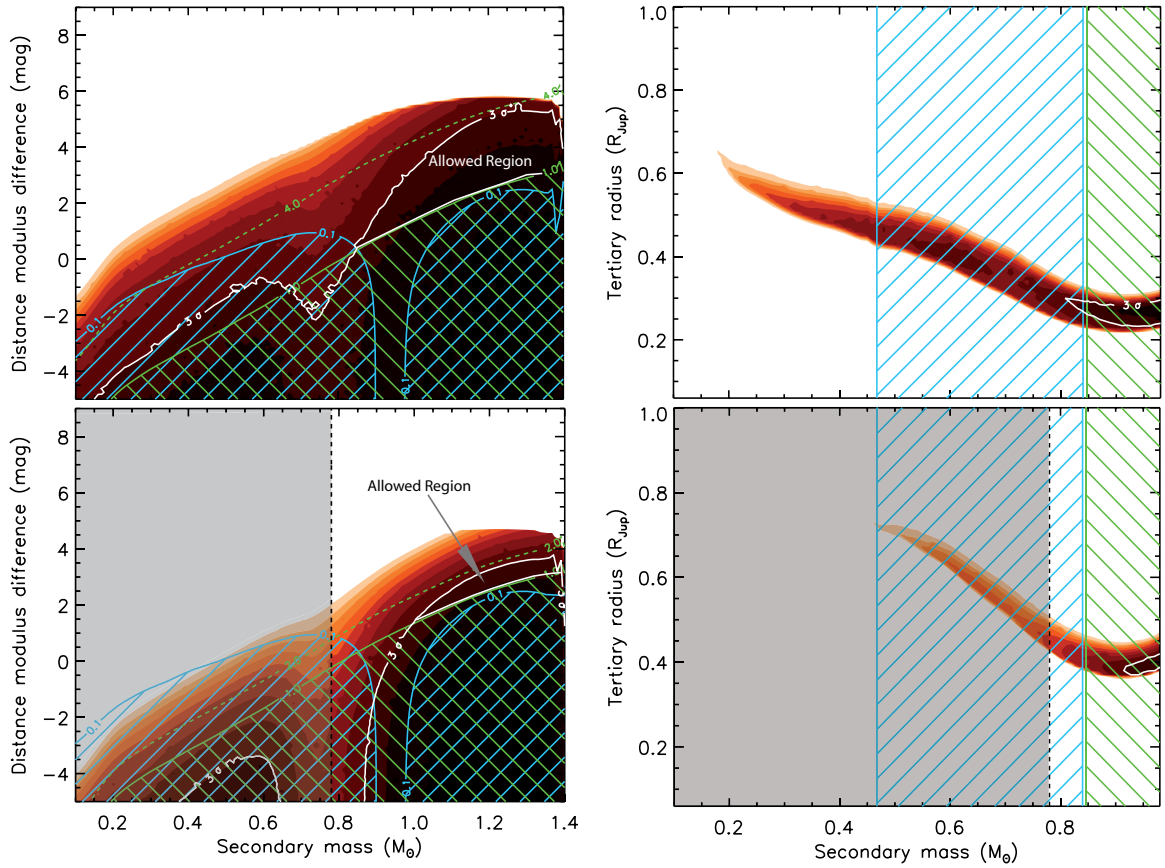

Figure 10. BLENDER constraints for Kepler-20b (top panels) and Kepler-20c (bottom), showing chance alignments with a star+planet pair on the left and physically associated stellar companions transited by a larger planet on the right. See Figure 9 for the meaning of the various lines. The space of parameters for background EBs is not shown as all of those scenarios provide very poor fits to the transit light curve and are ruled out. All blends involving physically associated stars transited by a larger planet (right panels) are excluded by a combination of spectroscopic constraints (specifically, on the absence of a secondary spectrum) and color constraints.

(A color version of this figure is available in the online journal.)

blends (i.e., the blend frequency) we expect a priori is reported in the last line of the table by adding these two numbers together and is approximately BF $= 6.0 \times 10^{-7}$.

We now compare this estimate with the likelihood that Kepler-20d is a true transiting planet (planet prior). To calculate the planet prior, we again make use of the census of 1235 candidates reported by Borucki et al. (2011) among the 156,453 *Kepler* targets observed during the first 4 months of operation of the Mission.[20] We count 100 candidates that are within 3σ of the measured radius ratio of Kepler-20d, implying an a priori transiting planet frequency of PF $= 100/156{,}453 = 6.4 \times 10^{-4}$. The likelihood of a planet is therefore several orders of magnitude larger than the likelihood of a false positive (PF/BF $= 6.4 \times 10^{-4}/6.0 \times 10^{-7} \approx 1100$), and we consider Kepler-20d to be validated as a planet with a high degree of confidence.

The transit signals from Kepler-20b and Kepler-20c are better defined, and as a result BLENDER is able to rule out all scenarios involving background EBs consisting of two stars, as well as all physically associated triples. This reduces the blend frequencies by one to two orders of magnitude compared to Kepler-20d. For Kepler-20c, *Spitzer* observations are available as well, although the constraints they provide are redundant with color information also available for the star, which already rules out contaminants of late spectral type. The areas of parameter space in which BLENDER finds false positives providing acceptable fits to the photometry are shown in Figure 10. The detailed calculations of the blend frequencies for Kepler-20b and Kepler-20c are presented in Tables 7 and 8, respectively, using appropriate ranges for the larger planets orbiting the blended stars as allowed by BLENDER, along with the corresponding transiting planet frequencies specified in the headings of Column 6.

Planet priors for these two candidates were computed as before using the catalog of Borucki et al. (2011). We count 52 cases in that list within 3σ of the measured radius ratio of Kepler-20b, leading to an a priori planet frequency of $52/156{,}453 = 3.3 \times 10^{-4}$. This is nearly 20,000 times larger than the blend frequency given in Table 7 (BF $= 1.7 \times 10^{-8}$). For Kepler-20c the planet prior based on the measured radius ratio is $28/156{,}453 = 1.8 \times 10^{-4}$, which is approximately 10^5 times larger than the likelihood of a blend. Therefore, both Kepler-20b and Kepler-20c are validated as planets with a very high degree of confidence.

We carried out similar calculations for the candidates K00070.04 and K00070.05. The transit signals of these two candidates are much more shallow than those of Kepler-20b, Kepler-20c, and Kepler-20d. As a result, the constraint on the shape of the transit is considerably weaker than in the cases

[20] While these 1235 candidates have not yet been confirmed as true planets, the rate of false positives is expected to be quite low (10% or less; see Morton & Johnson 2011), so our results will not be significantly affected by the assumption that all of the candidates are planets. We further assume here that the census of Borucki et al. (2011) is complete at these planetary radii.

Table 7
Blend Frequency Estimate for Kepler-20b (K00070.02)

		Blends Involving Planetary Tertiaries			
Kp Range (mag) (1)	ΔKp (mag) (2)	Stellar Density (per sq. deg) (3)	$\rho_{\max}$ ($''$) (4)	Stars ($\times 10^{-6}$) (5)	Blends ($\times 10^{-6}$) $R_p \in [0.27-1.81\ R_{\rm Jup}]$, $f_{\rm Plan} = 0.29\%$ (6)
12.5–13.0	0.5	...	...	...	...
13.0–13.5	1.0	...	...	...	...
13.5–14.0	1.5	271	0.075	0.370	0.00068
14.0–14.5	2.0	379	0.093	0.807	0.00149
14.5–15.0	2.5	404	0.11	1.185	0.00218
15.0–15.5	3.0	464	0.13	1.901	0.00351
15.5–16.0	3.5	498	0.15	2.716	0.00501
16.0–16.5	4.0	255	0.20	2.473	0.00456
16.5–17.0	4.5	...	...	...	...
17.0–17.5	5.0	...	...	...	...
17.5–18.0	5.5	...	...	...	...
18.0–18.5	6.0	...	...	...	...
18.5–19.0	6.5	...	...	...	...
19.0–19.5	7.0	...	...	...	...
19.5–20.0	7.5	...	...	...	...
20.0–20.5	8.0	...	...	...	...
Totals		2669	...	9.452	**0.0174**
Blend frequency (BF) $= 1.74 \times 10^{-8}$					

Note. Magnitude bins with no entries correspond to brightness ranges in which all blends are ruled out by a combination of BLENDER and other constraints.

Table 8
Blend Frequency Estimate for Kepler-20c (K00070.01)

		Blends Involving Planetary Tertiaries			
Kp Range (mag) (1)	ΔKp (mag) (2)	Stellar Density (per sq. deg) (3)	$\rho_{\max}$ ($''$) (4)	Stars ($\times 10^{-6}$) (5)	Blends ($\times 10^{-6}$) $R_p \in [0.39-1.95\ R_{\rm Jup}]$, $f_{\rm Plan} = 0.18\%$ (6)
12.5–13.0	0.5	...	...	...	...
13.0–13.5	1.0	...	...	...	...
13.5–14.0	1.5	221	0.075	0.300	0.00056
14.0–14.5	2.0	274	0.093	0.551	0.00108
14.5–15.0	2.5	...	...	...	...
15.0–15.5	3.0	...	...	...	...
15.5–16.0	3.5	...	...	...	...
16.0–16.5	4.0	...	...	...	...
16.5–17.0	4.5	...	...	...	...
17.0–17.5	5.0	...	...	...	...
17.5–18.0	5.5	...	...	...	...
18.0–18.5	6.0	...	...	...	...
18.5–19.0	6.5	...	...	...	...
19.0–19.5	7.0	...	...	...	...
19.5–20.0	7.5	...	...	...	...
Totals		495	...	0.851	**0.00164**
Blend frequency (BF) $= 1.64 \times 10^{-9}$					

Note. Magnitude bins with no entries correspond to brightness ranges in which all blends are ruled out by a combination of BLENDER and other constraints.

described above, and many more false positives than before are found with BLENDER that provide acceptable fits within 3σ of the quality of a planet model. Additionally, neither of these candidates was observed with *Spitzer*, so the constraint on the near-infrared depth of the transit that allowed us to rule out some of the blends for Kepler-20d is not available here. In particular, physically associated stars transited by a larger planet cannot all be ruled out, and this ends up contributing significantly to the overall blend frequency. We conclude that the BLENDER methodology as implemented above is insufficient to validate either K00070.04 or K00070.05, and we defer this issue to a subsequent study (Fressin et al. 2012b).

5. CONSTRAINTS ON TRANSIT TIMES AND LONG-TERM STABILITY

In this section, we discuss the transit times and long-term stability of the system of planets orbiting Kepler-20. Both are consistent with the planet interpretation for all five candidates:

Table 9
Transit Times for Kepler-20

ID	n	t_n BJD-2454900	TTV$_n$ (days)	σ_n (days)
Kepler-20b	$67.50027 + n \times 3.6961219$			
Kepler-20b	0	67.4942	−0.0061	0.0032
Kepler-20b	1	71.1956	−0.0008	0.0035
Kepler-20b	2	74.8946	0.0021	0.0041
Kepler-20b	3	78.5836	−0.0050	0.0035
Kepler-20b	4	82.2857	0.0009	0.0034
Kepler-20b	5	85.9768	−0.0040	0.0032
Kepler-20b	6	89.6783	0.0013	0.0045
Kepler-20b	7	93.3689	−0.0042	0.0037
Kepler-20b	8	97.0699	0.0007	0.0071
Kepler-20b	10	104.4602	−0.0012	0.0039

(This table is available in its entirety in a machine-readable form in the online journal. A portion is shown here for guidance regarding its form and content.)

TTVs (Holman & Murray 2005; Agol et al. 2005) are not seen or expected, and the system is expected to be stable over long timescales.

The individual transit times are measured by allowing a template transit light curve to slide in time to fit the data for each transit (Ford et al. 2011). The resulting transit times are given in Table 9. Aside from slightly more scatter than expected from the formal error bars, there is no indication of perturbations such as coherent patterns. Such excess scatter is not atypical of transit times measured by the standard pipeline (Ford et al. 2011). Thus, we find no evidence for dynamical interactions among either the transiting planets or additional, non-transiting planets.

To calculate predicted transit times, we numerically integrate our baseline model, which consists of a central star of mass 0.912 $M_\odot$ surrounded by planets with periods and epochs given in Table 2 (given at dynamical epoch BJD 2454170), and with masses of 8.7, 0.65, 16.1, 1.1, and 8.0 $M_\oplus$ (from least to greatest orbital period), corresponding to the best-fit masses for Kepler-20b and Kepler-20c, a guess of $M_p = M_\oplus\,(R_p/R_\oplus)^{2.06}$ (Lissauer et al. 2011a) for Kepler-20d, and masses giving Earth's density for K00070.04 and K00070.05. (We remind the reader that we have not, in this paper, validated these two candidates as planets. However, considering them as such for the purposes of evaluating dynamical stability is the conservative choice, since the presence of five planets, as opposed to three, is more likely to induce dynamical instabilities. Fressin et al. (2012b) present the validation of K00070.04 and K00070.05, give their sizes, from which the masses above are derived, and discuss constraints on their masses.) The orbits are chosen to be initially circular, coplanar, and edge-on to the line of sight. The rms deviations of the model transit times from the best-fit linear ephemeris projected over 8 years are approximately 3, 76, 9, 95, and 10 s (from least to greatest orbital period), all significantly smaller than the measurement precision shown in Figure 11.

Next, we investigated long-term stability for this system by integrating the baseline model with the hybrid algorithm in Mercury (Chambers 1999). As no close encounters were recorded, this algorithm reduced to the symplectic algorithm (Wisdom & Holman 1991), with time steps of 0.1 days, roughly 2.7% of the period of the innermost planet. Over the 10 Myr integration duration, there were no indications of instability. The orbital eccentricities fluctuated on the scale between approximately 3×10^{-5} (for Kepler-20d) and 0.001 (for K00070.04). We conclude that plausible, low-eccentricity models for the system are stable over long timescales.

Finally, we performed an ensemble of N-body integrations using the time-symmetric fourth-order Hermite integrator (Kokubo et al. 1998) implemented in `Swarm-NG`[21] to estimate the maximum plausible eccentricity for each planet consistent with long-term stability. For each N-body integration, we set four planets on circular orbits and assigned one planet a non-zero eccentricity. The eccentricity and pericenter directions for the planet on a non-circular orbit were drawn from uniform distributions. The maximum for the uniform distribution of eccentricities was chosen to be slightly larger than necessary for its orbit to cross one of its neighbors. We report $e_{\rm max}$, the maximum initial eccentricity that resulted in a system with no close encounters (within one mutual Hill radius) and semimajor axes (in a Jacobi frame) that varied by less than 1% for the duration of the integrations. Based on 100 integrations per planet and relatively short integrations (10^5 years), we estimate $e_{\rm max}$ to be 0.19, 0.16, 0.16, 0.38, and 0.55 (from smallest to largest orbital period). Technically, we cannot completely exclude larger eccentricities, due to various assumptions (such as the planet masses, coplanarity, prograde orbits, absence of false positives, and the potential for small islands of stability at higher eccentricity). Nevertheless, the N-body integrations support the assumption of non-crossing orbits, as the vast majority of systems with an eccentricity larger than $e_{\rm max}$ are dynamically unstable.

6. CONSTRAINTS ON THE PLANETARY COMPOSITIONS AND FORMATION HISTORY

The Kepler-20 system, harboring multiple sub-Neptune planets with constrained radii and masses, informs our understanding of both models of planet formation and the interior structure of planets that straddle the boundary between sub-Neptunes and super-Earths. The transit radii measured by *Kepler* and the planetary masses measured (or bounded) by RV observations together constrain the interior compositions of Kepler-20b, Kepler-20c, and Kepler-20d, as illustrated by the mass–radius diagram (Figure 12). We employ planet interior structure models (Rogers & Seager 2010; Rogers et al. 2011) to explore the range of plausible planet compositions. The interpretation is challenging because we do not yet know if these sub-Neptune planets had a stunted formation, or if they formed as gas giants and then lost significant mass to evaporation (Baraffe et al. 2004). This is partly owing to the uncertainties involved in atmospheric escape modeling.

Notably, both Kepler-20c and Kepler-20d require significant volatile contents to account for their low mean densities and cannot be composed of rocky and iron material alone. The volatile material in these planets could take the form of ices (H_2O, CH_4, NH_3) and/or H/He gas accreted during planet formation. Outgassing of rocky planets releases an insufficient quantity of volatiles (no more than 23% H_2O and 3.6% H_2 relative to the planet mass) to account for Kepler-20c and could account for Kepler-20d only in fine-tuned near-optimal outgassing scenarios (Elkins-Tanton & Seager 2008; Schaefer & Fegley 2008; Rogers et al. 2011). For Kepler-20c, ices (likely dominated by H_2O) would need to constitute the majority of its mass, in the absence of a voluminous, though low-mass, envelope of light gases. Alternatively, a composition with approximately 1% by mass H/He surrounding an Earth-composition refractory interior also matches the observed properties of the

[21] www.astro.ufl.edu/~eford/code/swarm/

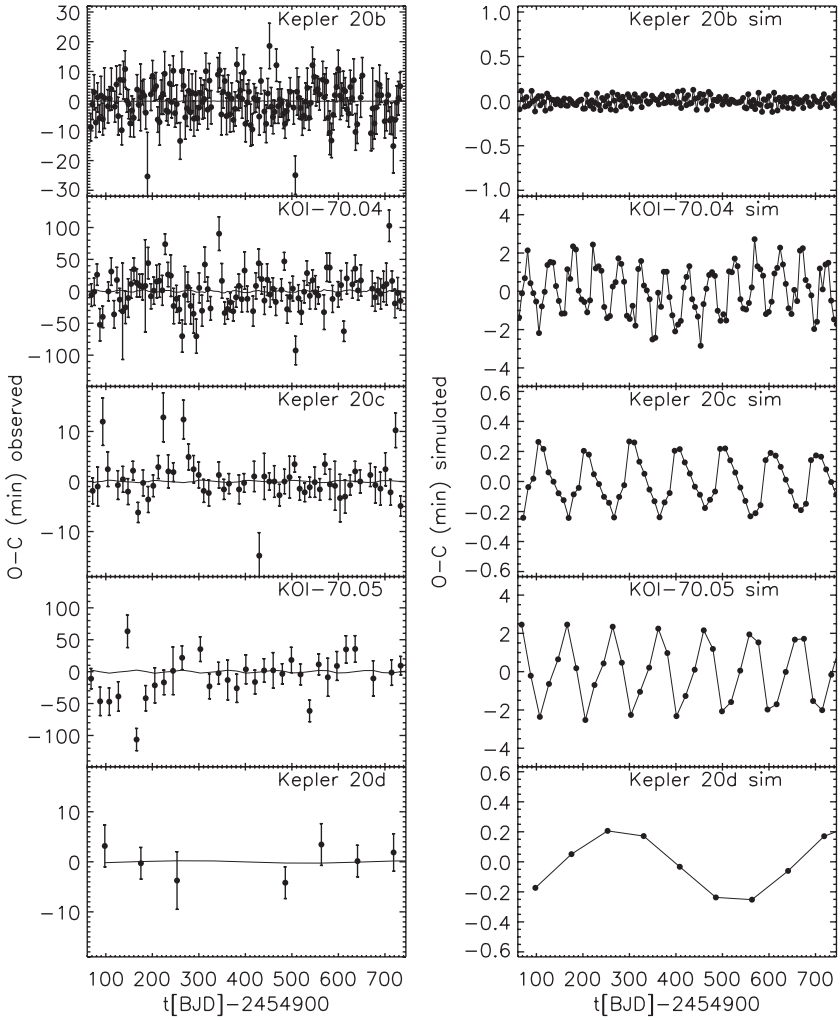

Figure 11. Measured and predicted transit timing for the planets of Kepler-20. Left panels: observed times minus calculated times according to a constant-period model ($O - C$) are plotted as points with error bars, vs. transit time. The timing simulations using circular, coplanar planets with nominal masses are plotted as lines. Right panels: the simulations are shown in more detail (30× zoom of each panel) to show the timescale and structure of variations.

planet within 1σ. Intermediate scenarios, wherein both H/He and higher mean molecular weight volatile species from ices contribute to the planet mass, are also possible. For Kepler-20d, the 2σ upper limit on the planet density demands at least a few percent H_2O by mass, or a few tenths of a percent H/He by mass.

The nature of Kepler-20b's composition is ambiguous: Kepler-20b could be terrestrial (with the transit radius defined by a rocky surface), or it could support a significant gas envelope (like Kepler-20c and Kepler-20d). In the mass–radius diagram (Figure 12), the measured properties of Kepler-20b straddle the pure-silicate composition curve that defines a strict upper bound to rocky planet radii. If Kepler-20b is in fact a terrestrial planet consisting of an iron core surrounded by a silicate mantle, the 1σ limits on the planet mass and radius constrain the iron core to be less than 62% of the planet mass. In particular, an Earth-like composition (30% iron core, 70% silicate mantle) is possible and matches the observational constraints to within 1σ, but a Mercury-like composition (70% iron core, 30% silicate mantle) is not acceptable. Alternatively, Kepler-20b may harbor a substantial gas layer like its sibling planets Kepler-20c and Kepler-20d at larger orbital semimajor axes and/or contain a significant component of astrophysical ices such as H_2O. The 1σ lower limits on the planet density constrain the fraction of Kepler-20b's mass that can be contributed by H_2O ($\lesssim$55%) and H/He ($\lesssim$1%).

Given their high levels of stellar irradiation (the semimajor axes of all five Kepler-20 planets are smaller than that of Mercury), atmospheric escape likely played an important role in sculpting the compositions of the Kepler-20 planets. Planet compositions with low mean molecular weight gas envelopes would be especially susceptible to mass loss. Using a model for energy-limited escape from hydrogen-rich envelopes (Lecavelier Des Etangs 2007), we estimate that Kepler-20b would be losing on the order of $4 \times 10^6\,\mathrm{kg\,s^{-1}}$, which corresponds to $0.02\ M_\oplus\,\mathrm{Gyr}^{-1}$. Following the same approach, the estimated hydrogen mass-loss rates for Kepler-20c and Kepler-20d are $2 \times 10^6\,\mathrm{kg\,s^{-1}}$ ($0.01\ M_\oplus\,\mathrm{Gyr}^{-1}$) and $8 \times 10^4\,\mathrm{kg\,s^{-1}}$ ($0.0004\ M_\oplus\,\mathrm{Gyr}^{-1}$), respectively. Our theoretical understanding of atmospheric escape from highly irradiated super-Earth and sub-Neptune exoplanets is very uncertain, and higher mass-loss rates are plausible (especially at earlier times when the host star was more active). It is intriguing that Kepler-20b, with its shorter orbital period and greater vulnerability to mass loss, also has a higher mean density than Kepler-20c and Kepler-20d. More detailed modeling may constrain Kepler-20b's compositional history and the extent to which its relative paucity of volatiles can be attributed to evaporation.

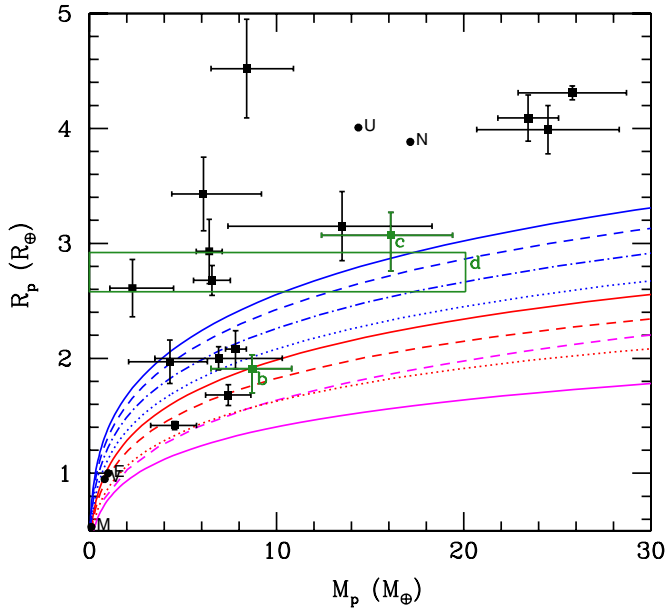

Figure 12. Mass–radius relationships of small transiting planets. The three confirmed planets in the Kepler-20 system are highlighted in green. Kepler-20b and Kepler-20c are plotted with error bars delimiting the 1σ uncertainties on the planet mass and radius, while Kepler-20d is plotted with bands illustrating the 2σ mass upper limit. Other small transiting exoplanets with measured masses (Kepler-10b, CoRoT-7b, Kepler-11bcdef, Kepler-18b, 55Cnc e, GJ 1214b, HD 97658b, GJ 436b, Kepler-4b, HAT-P-11b) are plotted in black. The solar system planets are indicated with the first letters of their names. The curves are illustrative constant-temperature (300 K) mass–radius relations for bodies devoid of H/He from Seager et al. (2007). The solid lines are homogeneous-composition planets: water ice (blue solid), $MgSiO_3$ perovskite (red solid), and iron (magenta solid). The non-solid lines are mass–radius relations for differentiated planets: 75% water ice, 22% silicate shell, and 3% iron core (blue dashed); Ganymede-like with 45% water ice, 48.5% silicate shell, and 6.5% iron core (blue dot-dashed); 25% water ice, 52.5% silicate shell, and 22.5% iron core (blue dotted); Earth-like with 67.5% silicate mantle and 32.5% iron core (red dashed); and Mercury-like with 30% silicate mantle and 70% iron core (red dotted). The minimal radius curve based on simulations of collisional mantle stripping from differentiated silicate-iron planets (Marcus et al. 2010) is denoted by the dashed magenta line.

(A color version of this figure is available in the online journal.)

The Kepler-20 planetary system shares several remarkable attributes with Kepler-11 (Lissauer et al. 2011a), namely, the presence of multiple transiting low-density low-mass planets in a closely spaced orbital architecture. The Kepler-20 system is less extreme than Kepler-11 in the realms of both low planet densities (Figure 12) and dynamical compactness (the Kepler-11 planets exhibit TTVs while the Kepler-20 planets do not).

A striking feature of the Kepler-20 planetary system is the presence of Earth-size rocky planet candidates interspersed between volatile-rich sub-Neptunes at smaller and larger orbital semimajor axes, as also seen in *Kepler* candidate multi-planet systems (Lissauer et al. 2011b). Assuming that both K00070.04 and K00070.05 are planets, the distribution of the Kepler-20 planets in orbital order is as follows: Kepler-20b (3.7 days, 1.9 $R_\oplus$), K00070.04 (6.1 days, 0.9 $R_\oplus$), Kepler-20c (10.9 days, 3.1 $R_\oplus$), K00070.05 (19.6 days, 1.0 $R_\oplus$), and Kepler-20d (77.6 days, 2.8 $R_\oplus$). Given the radii and irradiation fluxes of the two Earth-size planet candidates, they would not retain gas envelopes. The first, second, and fourth planets have high densities indicative of solid planets, while the other two planets have low densities requiring significant volatile content. The volatile-rich third planet, Kepler-20c, dominates the inner part of the Kepler-20 system, by holding much more mass than the other three inner planets put together. In the solar system, the terrestrial planets, gas giants, and ice giants are neatly segregated in regions with increasing distance from the Sun. Planet formation theories were developed to retrodict these solar system composition trends (e.g., Safronov 1969; Chambers 2010; D'Angelo et al. 2010). In the Kepler-20 system, the locations of the low-density sub-Neptunes that are rich in water and/or gas and the Earth-size planet candidates do not exhibit a clean ordering with orbital period, challenging the conventional planet formation paradigm. In situ assembly may form multi-planet systems with close-in hot-Neptunes and super-Earths, provided that the initial protoplanetary disk contained massive amounts of solids (~50–100 $M_\oplus$) within 1 AU of the star (Hansen & Murray 2011).

Kepler was competitively selected as the tenth Discovery mission. Funding for this mission is provided by NASA's Science Mission Directorate. The authors thank many people who gave so generously of their time to make this mission a success. This work is also based in part on observations made with the *Spitzer Space Telescope*, which is operated by the Jet Propulsion Laboratory, California Institute of Technology under a contract with NASA. Support for this work was provided by NASA through an award issued by JPL/Caltech. We thank the *Spitzer* staff at IPAC and in particular Nancy Silbermann for scheduling the *Spitzer* observations of this program. Some of the data presented herein were obtained at the W. M. Keck Observatory, which is operated as a scientific partnership among the California Institute of Technology, the University of California, and the National Aeronautics and Space Administration. The Observatory was made possible by the generous financial support of the W. M. Keck Foundation.

REFERENCES

Adams, E. R., Seager, S., & Elkins-Tanton, L. 2008, ApJ, 673, 1160
Agol, E., Steffen, J., Sari, R., & Clarkson, W. 2005, MNRAS, 359, 567
Ballard, S., Fabrycky, D., Fressin, F., et al. 2011, ApJ, 743, 200
Baraffe, I., Selsis, F., Chabrier, G., et al. 2004, A&A, 419, L13
Basri, G., Walkowicz, L. M., Batalha, N., et al. 2010, ApJ, 713, L155
Basri, G., Walkowicz, L. M., Batlaha, N., et al. 2011, AJ, 141, 20
Batalha, N. M., Borucki, W. J., Bryson, S. T., et al. 2011, ApJ, 729, 27
Batalha, N. M., Rowe, J. F., Gilliland, R. L., et al. 2010, ApJ, 713, L103
Borucki, W. J., Koch, D., Basri, G., et al. 2010, Science, 327, 977
Borucki, W. J., Koch, D. G., Basri, G., et al. 2011, ApJ, 736, 19
Brown, T. M., Latham, D. W., Everett, M. E., & Esquerdo, G. A. 2011, AJ, 142, 112
Bryson, S. T., Tenenbaum, P., Jenkins, J. M., et al. 2010, ApJ, 713, L97
Buchhave, L. A., Bakos, G. Á., Hartman, J. D., et al. 2010, ApJ, 720, 1118
Buchhave, L. A., Latham, D. W., Carter, J. A., et al. 2011, ApJS, 197, 3
Butler, R. P., Marcy, G. W., Fischer, D. A., et al. 1999, ApJ, 526, 916
Caldwell, D. A., Kolodziejczak, J. J., Van Cleve, J. E., et al. 2010, ApJ, 713, L92
Chambers, J. 2010, Exoplanets, ed. S. Seager (Tucson, AZ: Univ. Arizona Press), 297
Chambers, J. E. 1999, MNRAS, 304, 793
Charbonneau, D., Allen, L. E., Megeath, S. T., et al. 2005, ApJ, 626, 523
Charbonneau, D., Brown, T. M., Latham, D. W., & Mayor, M. 2000, ApJ, 529, L45
Charbonneau, D., Brown, T. M., Noyes, R. W., & Gilliland, R. L. 2002, ApJ, 568, 377
Claret, A., & Bloemen, S. 2011, A&A, 529, A75
Cochran, W. D., Fabrycky, D. C., Torres, G., et al. 2011, ApJS, 197, 7
D'Angelo, G., Durisen, R. H., & Lissauer, J. J. 2010, Exoplanets, ed. S. Seager (Tucson, AZ: Univ. Arizona Press), 319
Demarque, P., Woo, J.-H., Kim, Y.-C., & Yi, S. K. 2004, ApJS, 155, 667
Désert, J.-M., Charbonneau, D., Fortney, J. J., et al. 2011a, ApJS, 197, 11
Désert, J.-M., Lecavelier des Etangs, A., Hébrard, G., et al. 2009, ApJ, 699, 478
Désert, J.-M., Sing, D., Vidal-Madjar, A., et al. 2011b, A&A, 526, A12

Djupvik, A. A., & Andersen, J. 2010, Highlights of Spanish Astrophysics V (Berlin: Springer), 211
Elkins-Tanton, L. T., & Seager, S. 2008, ApJ, 685, 1237
Fazio, G. G., Hora, J. L., Allen, L. E., et al. 2004, ApJS, 154, 10
Ford, E. B., Lystad, V., & Rasio, F. A. 2005, Nature, 434, 873
Ford, E. B., Rowe, J. F., Fabrycky, D. C., et al. 2011, ApJS, 197, 2
Fressin, F., Torres, G., Désert, J.-M., et al. 2011, ApJS, 197, 5
Fressin, F., Torres, G., Pont, F., et al. 2012a, ApJ, 745, 81
Fressin, F., Torres, G., Rowe, J. F., et al. 2012b, Nature, 482, 195
Gilliland, R. L., Jenkins, J. M., Borucki, W. J., et al. 2010, ApJ, 713, L160
Gregory, P. C. 2011, MNRAS, 410, 94
Hansen, B. M. S., & Murray, N. 2011, arXiv:1105.2050
Hayward, T. L., Brandl, B., Pirger, B., et al. 2001, PASP, 113, 105
Henry, G. W., Marcy, G. W., Butler, R. P., & Vogt, S. S. 2000, ApJ, 529, L41
Holman, M. J., Fabrycky, D. C., Ragozzine, D., et al. 2010, Science, 330, 51
Holman, M. J., & Murray, N. W. 2005, Science, 307, 1288
Horch, E. P., Gomez, S. C., Sherry, W. H., et al. 2011, AJ, 141, 45
Howell, S. B., Everett, M. E., Sherry, W., Horch, E., & Ciardi, D. R. 2011, AJ, 142, 19
Howell, S. B., Rowe, J. F., Bryson, S. T., et al. 2012, ApJ, 746, 123
IRAC Instrument and Instrument Support Teams 2011, IRAC Instrument Handbook v2.0.1 (NASA/IPAC Infrared Science Archive), 45
Isaacson, H., & Fischer, D. 2010, ApJ, 725, 875
Jenkins, J. M., Borucki, W. J., Koch, D. G., et al. 2010a, ApJ, 724, 1108
Jenkins, J. M., Caldwell, D. A., Chandrasekaran, H., et al. 2010b, ApJ, 713, L87
Jenkins, J. M., Caldwell, D. A., Chandrasekaran, H., et al. 2010c, ApJ, 713, L120
Jenkins, J. M., Smith, J. C., Tenenbaum, P., Twicken, J. D., & Van Cleve, J. 2011, in Advances in Machine Learning and Data Mining for Astronomy, ed. M. Way, J. Scargle, K. Ali, & A. Srivastava (London: Chapman and Hall/CRC)
Johnson, J. A., Clanton, C., Howard, A. W., et al. 2011, ApJS, 197, 26
Knutson, H. A., Charbonneau, D., Allen, L. E., Burrows, A., & Megeath, S. T. 2008, ApJ, 673, 526
Knutson, H. A., Charbonneau, D., Allen, L. E., et al. 2007, Nature, 447, 183
Koch, D. G., Borucki, W. J., Basri, G., et al. 2010, ApJ, 713, L79
Kokubo, E., Yoshinaga, K., & Makino, J. 1998, MNRAS, 297, 1067
Latham, D. W., Rowe, J. F., Quinn, S. N., et al. 2011, ApJ, 732, L24
Lecavelier Des Etangs, A. 2007, A&A, 461, 1185
Lee, M. H., & Peale, S. J. 2002, ApJ, 567, 596
Lissauer, J. J., Fabrycky, D. C., Ford, E. B., et al. 2011a, Nature, 470, 53
Lissauer, J. J., Ragozzine, D., Fabrycky, D. C., et al. 2011b, ApJS, 197, 8
Lloyd, J. P., Liu, M. C., Macintosh, B. A., et al. 2000, Proc. SPIE, 4008, 814
Malhotra, R. 2008, ApJ, 575, L33
Mamajek, E. E., & Hillenbrand, L. A. 2008, ApJ, 687, 1264
Mandel, K., & Agol, E. 2002, ApJ, 580, L171
Marcus, R. A., Sasselov, D., Hernquist, L., & Stewart, S. T. 2010, ApJ, 712, L73
Mayor, M., Marmier, M., Lovis, C., et al. 2011, arXiv1109.2497
Miller, N., & Fortney, J. J. 2011, ApJ, 736, L29
Morton, T. D., & Johnson, J. A. 2011, ApJ, 738, 170
Noyes, R. W., Hartmann, L. W., Baliunas, S. L., Duncan, D. K., & Vaughan, A. H. 1984, ApJ, 279, 763
Rasio, F. A., Nicholson, P. D., Shapiro, S. L., & Teukolsky, S. A. 1992, Nature, 355, 325
Robin, A. C., Reylé, C., Derrière, S., & Picaud, S. 2003, A&A, 409, 523
Rogers, L. A., Bodenheimer, P., Lissauer, J. J., & Seager, S. 2011, ApJ, 738, 59
Rogers, L. A., & Seager, S. 2010, ApJ, 716, 1208
Safronov, V. S. 1969, Evoliutsiia Doplanetnogo Oblaka (Moscow: Nauka)
Schaefer, L., & Fegley, B. 2008, Meteorit. Planet. Sci. Suppl., 43, 5037
Seager, S., Kuchner, M., Hier-Majumder, C. A., & Militzer, B. 2007, ApJ, 669, 1279
Slawson, R. W., Prša, A., Welsh, W. F., et al. 2011, AJ, 142, 160
Steffen, J. H., Batalha, N. M., Borucki, W. J., et al. 2010, ApJ, 725, 1226
Ter Brakk, C. J. F. 2006, Stat. Comput., 16, 239
Torres, G., Fressin, F., Batalha, N. M., et al. 2011, ApJ, 727, 24
Torres, G., Konacki, M., Sasselov, D. D., & Jha, S. 2004, ApJ, 614, 979
Torres, G., Neuhäuser, R., & Guenther, E. W. 2002, AJ, 123, 1701
Triaud, A. H. M. J., Collier Cameron, A., Queloz, D., et al. 2010, A&A, 524, 25
Troy, M., Dekany, R. G., Brack, G., et al. 2000, Proc. SPIE, 4007, 31
Valenti, J. A., & Fischer, D. A. 2005, ApJS, 159, 141
Valenti, J. A., & Piskunov, N. 1996, A&A, 118, 595
Van Cleve, J., & Caldwell, D. A. 2009, Kepler Instrument Handbook (KSCI 19033-001; Moffett Field, CA: NASA Ames Research Center)
Vogt, S. S., Allen, S. L., Bigelow, B. C., et al. 1994, Proc. SPIE, 2198, 362
Werner, M. W., Roellig, T. L., Low, F. J., et al. 2004, ApJS, 154, 1
Winn, J. N. 2010, in Exoplanets, ed. S. Seager (Tucson, AZ: Univ. Arizona Press), 55
Wisdom, J., & Holman, M. 1991, AJ, 102, 1528
Wolszczan, A. 1994, Science, 264, 538
Wolszczan, A., & Frail, D. A. 1992, Nature, 355, 145
Yi, S., Demarque, P., Kim, Y.-C., et al. 2001, ApJS, 136, 417